Combustion and Flame 266 (2024) 113537

Contents lists available at ScienceDirect

Combustion and Flame

journal homepage: www.sciencedirect.com/journal/combustion-and-flame

The Planar Mixing Layer Flame (PMLF): a canonical configuration for studying non-premixed combustion chemistry and soot inception

Mahmoud K. Ashour, Francesco Carbone *

School of Mechanical, Aerospace, and Manufacturing Engineering, University of Connecticut, 191 Auditorium Road, Unit 3139, Storrs, CT 06269, USA

ARTICLE INFO

Keywords:
Laminar non-premixed flames
Polycyclic aromatic hydrocarbons (PAHs)
Soot
Capillary sampling for GC/MS
Combustion chemistry

ABSTRACT

The study of fuel chemistry and soot inception in non-premixed combustion can be advanced by characterizing flame configurations in which the advection and diffusion transport can be finely controlled, with the ability to decouple pyrolysis from oxidation. Also, the ideal flames to be investigated should be perturbed minimally by probes and thick enough for sampling techniques to yield spatially resolved measurements of their structure. The Planar Mixing Layer Flame (PMLF) configuration introduced herein is established between a fuel and an oxidizer slot jet adjacent to each other and shielded from the ambient air by annularly co-flowing inert nitrogen. The PMLF flow is kept laminar and steady by an impinging flat plate equipped with a rectangular exhaust slit opening which anchors the position of the hot combustion products via buoyancy. The PMLF is accessible to sampling and its flow stability is preserved when using any tested probe. The experiments are complemented with 2D-Computational Fluid Dynamics (CFD) modeling with detailed chemical kinetics. The results demonstrate that the PMLF has a self-similar boundary layer structure whose horizontal cross-sections are equivalent to properly selected and equally thick 1D- Counterflow Flames (CFs). The equivalence allows for excellent predictions of the PMLF thermochemical structure characterized experimentally but at a small fraction of the 2D-CFD computational cost. The 1D-CF equivalence affects even aromatics less than twofold despite their kinetics being known to be very sensitive to the temperature field. Importantly, the PMLF thickness is several millimeters and grows at increasing HABs so that the equivalent 1D-CFs have strain rates as small as 7.0 /s which cannot be studied in CF experiments. As a result, the PMLF emerges as a promising canonical non-premixed flame configuration for studying flame chemistry and soot inception on time scales of tens of milliseconds typical of many combustion applications.

Novelty and Significance Statement

This study introduces a novel canonical configuration for laminar non-premixed flame studies that results from a substantial variant of the original Wolfhard-Parker design. The innovation consists of a mixed impinging flow and buoyancy-driven stabilization method that enable the study of an unconfined Planar Mixing Layer Flame (PMLF), minimally perturbed by sampling and with very mild spatial gradients. The PMLF has advection times of several tens of milliseconds typical of many combustion applications and couples some of the advantages of Counter-Flow (CF) and co-flow flame configurations in terms of both the range of experimentally accessible conditions and ease of interpretation of results. Also, the PMLF has well-defined boundary conditions that ease its 2D-CFD modeling, and the structures of its horizontal cross sections are equivalent to 1D-CFs with strain rates much lower than achievable in CF experiments. The equivalence enables approximate 1D modeling at a small fraction of the 2D-CFD computational cost. In brief, this and ensuing studies of the PMLF configuration can be instrumental to improving detailed chemical kinetic models and unraveling the mechanisms of soot inception in non-premixed flames.

1. Introduction

Specialized agencies forecast carbon-based fuels to dominate the satisfaction of the energy demand in the United States and the rest of the world at least until the middle of this century [1–3]. Meanwhile, governmental restrictions on the environmental impact of combustion

* Corresponding author.
E-mail address: carbone@uconn.edu (F. Carbone).

https://doi.org/10.1016/j.combustflame.2024.113537
Received 20 November 2023; Received in revised form 26 May 2024; Accepted 28 May 2024

push the research community to develop technologies with ever-reduced emissions and -enhanced efficiency. Soot is a main by-product of the combustion of carbon-containing fuels with significant effects on both human health [4–8] and climate [9]. Soot formation has been a focus of research for more than five decades [10–36], which generated a wealth of knowledge about the many stages of the process. Still, the mechanisms of soot inception which is the step leading to the transition from the gas to the condensed phase, remain unclear and the role Polycyclic Aromatics Hydrocarbons (PAHs) play in this step is an object of intense debate in the scientific community [24,25,28–36].

The study of combustion chemistry and soot formation in practical combustion applications is limited by several "complications" such as the use of complex fuel blends, turbulent flow, and atomization and evaporation of multicomponent sprays. Instead, the identification of cause-and-effect relationships is simplified greatly in canonical laminar flames of pre-vaporized pure fuel mixtures in which fluid mechanics are simple but the oxidation and pyrolysis chemistry retains all its complexity. The most common canonical configurations used for studying non-premixed combustion are the Axisymmetric co-flow Flame (AcoF) and the Counterflow Flame (CF).

AcoFs are easy to stabilize on relatively inexpensive burners and enable the investigation of the effect of advection times of tens of milliseconds, relevant to most applications. Therefore, AcoFs have been used in a plethora of (soot formation) studies [e.g.,15,17,22,37–39], including some at quite high pressure (p) [e.g.,11,26]. Unfortunately, quantitative concurrent measurements of the gas components and soot in AcoFs are rare [e.g.,17] and lack the spatial resolution necessary to unravel the flame structure. Indeed the inherent spatial averaging caused by sampling techniques is disruptive when the isosurfaces of the fields to be measured have radiii of curvature comparable to the size of the sampled volume [15,40]. The limitations are amplified for AcoFs at increasing p which get increasingly thinner and prone to suffer flow instabilities due to buoyancy [26]. Last but not least, the thermochemical-advection histories vary broadly along different gas streamlines within the same AcoF and buoyancy amplifies the differences between ACoFs at different p and/or maximum temperatures (T_{max}) [10]. The best evaluation of the effects of p in ACoFs can be performed only by comparing AcoFs that have the same height and reactant velocity (and, therefore, different T_{max}). In these cases, only an average of the global advection time can be kept approximately constant [26]. The difficulty of performing detailed comparisons of different results in AcoFs persists even if one overlooks the hurdles, amplified at high p, of achieving well-defined and ideally adiabatic boundary conditions [e.g.,37]. Last, AcoFs do not allow for investigating the effect of flame stretch (or, equivalently, strain rate, and/or scalar dissipation rate) nor decoupling pyrolysis from oxidation along different gas streamlines. In brief, the identification of cause-and-effect relationships from results in different AcoFs is very difficult and ambiguous.

The CF configuration has been playing a significant role in studying non-premixed flames since its introduction in the sixties because it overcomes many limitations of AcoFs [41]. In the first place, the asymptotic 1D self-similar structure of CFs [42] can mimic the local structure of a variety of non-premixed flames including turbulent ones [43–46]. Well-controlled CFs can be obtained at several p for several fuel blends and under a broad range of values of the parameters controlling its structure [14,16,23,29,47–54]. For example, the fuel and oxidizer velocities (u_F and u_{Ox}, respectively) and the nozzle separation distance (L) determine a global strain rate value [47] (e.g., $a=[u_F+u_{Ox}]/L$) and the fuel and oxidizer compositions influence the stoichiometric mixture fraction (Z_{st}) [16,29] and T_{max} [29,50–52]. Of course, p and T_{max} affect the chemical reaction rates whereas, for a given burner geometry, a determines the spatial distribution of the local flame strain rate (a') which controls the advection and diffusion transport, determining the flame thickness [47,49–51]. On the other hand, Z_{st} determines the position of the oxidation layer relative to the Gas Stagnation Plane (GSP) [16] and, in turn, the achievement of either exclusively pyrolytic (i.e., soot formation) or combined pyrolytic-oxidative (i.e., soot formation and oxidation) conditions in the fuel stream and flame soot-laden zone for $Z_{st}<0.5$ or $Z_{st}>0.5$, respectively [16]. Therefore, one should perform studies of the effect of changing a, Z_{st}, and T_{max} to unravel the chemical complexity of any diffusion flame, or at least bear in mind changes in their values when comparing results obtained in different CFs [29,36]. A judicious selection of a, Z_{st}, p, and T_{max} in the range that avoids 2D effects enables the achievement of constant thermochemical advection and diffusion transport histories along most gas streamlines yielding from either the fuel or oxidizer nozzle [36,49–52,55]. Additionally, when a (precisely the a' field) and Z_{st} are kept constant while changing either p and/or T_{max}, the flame structure stays self-similar [51–53,56] with constant advection histories of the reduced [57] profiles of Temperature (T) and mole fractions (X_i) of all of the i-species. In this way, one can isolate the effect of p and T_{max} [51–56] on the reaction kinetics determining the maximum mole fraction ($X_{i,\max}$) of each combustion intermediate. Studies of this type in non-premixed and partially premixed CFs with $Z_{st}=0.183$ relied on capillary sampling followed by chemical analyses of gaseous species complemented by in-situ optical characterization of soot and showed that soot inception in ethylene-fueled flames may be controlled by small aromatics [32,36,50–56].

Unfortunately, CFs also have some limitations the first of which is their inaccessibility to intrusive dilution and thermophoretic sampling used to measure the Particle Size Distribution Function (PSDF) of soot with DMA/SMPS [58-60] and microscopy techniques [61], respectively. Indeed, the elliptic nature of the CF governing equations causes cold probes to perturb the entire flame structure. The perturbation effects can be so severe that some scientists are skeptical even about the accuracy of capillary sampling the gas products along a thermochemical isosurface [15] with a probe that is very thin (<0.35 mm) and almost at the same T as the sampled flame layer [49]. Nevertheless, the literature reports a couple of attempts to implement dilution sampling using a cold and (~6 mm) bulky quartz probe to sample the CF products from different flame layers and measure the soot PSDF but the spatial resolution ot the approach is unassessed [62,63]. These attempts consider CFs with relatively large soot loads and average particle sizes and do not track materials smaller than 3 nm that are those to study if one wants to unravel the mechanisms of soot inception but also the most difficult to measure with spatial resolution and without artifacts [30–33,36]. Last, a in CF experiments must be larger than at least 25 $/s$ to avoid flow buoyant instabilities and substantial effects of radial mass and heat transfer which can lead to perturbation of the 1D-CF self-similar thermochemical structure [47,64,65]. As a result, CFs not only cannot be made arbitrarily thick to counteract the intrusiveness of sampling but also pose experimental limits on the longest global advection time (which is inversely proportional to a) available for the slowest flame chemical kinetics to manifest their effects measurably.

In 1949 Wolfhard and Parker (WP) [66] used a planar non-premixed flame configuration whose cross sections are thick enough to perform spatially resolved in-situ spectroscopy measurements. Their flame is established near the interface between two adjacent planar co-flow jets, one yielding the fuel and the other oxygen. They used nitrogen shielding to isolate the two reactant streams from the surroundings and enclosed the burner in a vessel equipped with quartz windows for optical access. In the original WP design, the enclosure is essential to minimize any perturbation of the flame that triggers the flow instabilities inherent to the configuration, and to keep the flame laminar at Heights Above the Burner (HABs) up to 12 mm where measurements are performed. The WP flame configuration benefits from all the advantages of the CFs and overcomes most of its limitations at the cost of the complete loss of accessibility for sampling. This is not only because of the enclosure but also because the insertion of a sampling probe would trigger flickering which prevents any sampling with spatial resolution. To leverage some advantages of the planar WP flames and overcome their stability limitations, Kent et al. [13] modified the WP design by sandwiching the fuel

jet between two air jets surrounded by shielding nitrogen to establish a Planar co-flow Flame (PcoF). The modifications coupled with the installation of a contraction at the top of the burner made of a pair of wire gauze, minimize flame flickering and enhance the stability of two planar flame sheets at large HABs. This modification enables sampling the flame products at HAB up to 45 mm with some spatial resolution using quartz probes to perform analyses with mass spectrometry (MS) [37,67–72]. As a drawback, the PcoF design does not allow for the decoupling of oxidation and pyrolysis along different gas streamlines and is not suitable for simple computational modeling because of the complicated gauze wire geometry [37]. The literature compared the structure of a PcoF to that of an AcoF with the same reactant composition [13,37]. To overcome the geometrical differences, and inspired by the flamelet approaches, the authors utilized geometry-independent parameters such as mixture fraction and scalar dissipation rate. They recommended extending the comparison to CFs [37], a task that has not yet been completed.

In this work, we introduce a novel modification of the original WP design which relies on a passive stabilization technique resulting in the Planar Mixing Layer Flame (PMLF) configuration. The modification leverages the buoyancy of the hot flame products to anchor the flame to an exhaust slit perforated in a stagnation plate installed downstream of the burner nozzles without the need for an enclosure. The investigated incipiently soot-forming PMLF is stable even when one inserts into it a capillary sampling probe, a thin thermocouple, or a bulky horizontal tube dilution sampling probe to characterize its structure. The PMLF is adaptable to high-pressure studies of diffusion and partially premixed flames fueled by several pre-vaporized fuels. Last but not least, the unperturbed PMLF can be modeled easily by 2D-CFD and its horizontal cross-sections have a self-similar structure that is the same as that of an equivalent 1D-CFs with a as small as 7.0 /s.

2. Experimental and computational modeling methods

2.1. The Planar Mixing Layer Flame (PMLF): burner design and test conditions

Fig. 1 shows a cross-section of the Planar Mixing Layer Flame (PMLF) burner. It consists of two adjacent and identical slot nozzles with 25 mm by 50 mm rectangular cross-sections. The left and right nozzles deliver laminar plug flow jets of the fuel and the oxidizer mixtures, respectively. The two nozzles are surrounded by a 12 mm wide rectangular annulus for flowing nitrogen which shields the jets of the reactants from the surrounding air. The burner interior is filled with glass beads and layered fiberglass padding, and wire meshes are installed at the outlets of the nozzles and annulus to achieve the desired laminar plug flow boundary conditions. A stainless-steel plate with a rectangular slit opening whose position and width are adjustable using two shim stocks, is installed orthogonally to the flow at HAB=80 mm. The slit is necessary to exhaust the hot flame products while the surrounding cold flow impinges on the plate. To achieve the best flow stability, the plate slit opening must be as small as possible to anchor the hot stream of the PMLF burnt products via buoyancy but large enough to exhaust all such hot products without plate heating. Also, the stabilization plate slit has to be centered near the horizontal maximum Temperature (T_{max}) which is positioned off-axis since stoichiometric conditions are established in either one of the fuel or oxidizer streams according to the selected value of the stoichiometric mixture fraction (Z_{st}).

The optimal slit width and position depend on the boundary conditions of the PMLF and have to be determined by trial and error via flame digital imaging with or without the assistance of computational modeling. The PMLF investigated herein is fueled by ethylene and has Z_{st}=0.183 as in a variety of literature studies on CFs [50–56]. The velocities of the cold (i.e., nominally 298 K) fuel, oxidizer, and shielding nitrogen streams are $V_F = V_{Ox} = V_{N2} = 0.20$ m/s. The ethylene and oxygen mole fractions in the nitrogen-diluted fuel and oxidizer streams are set to

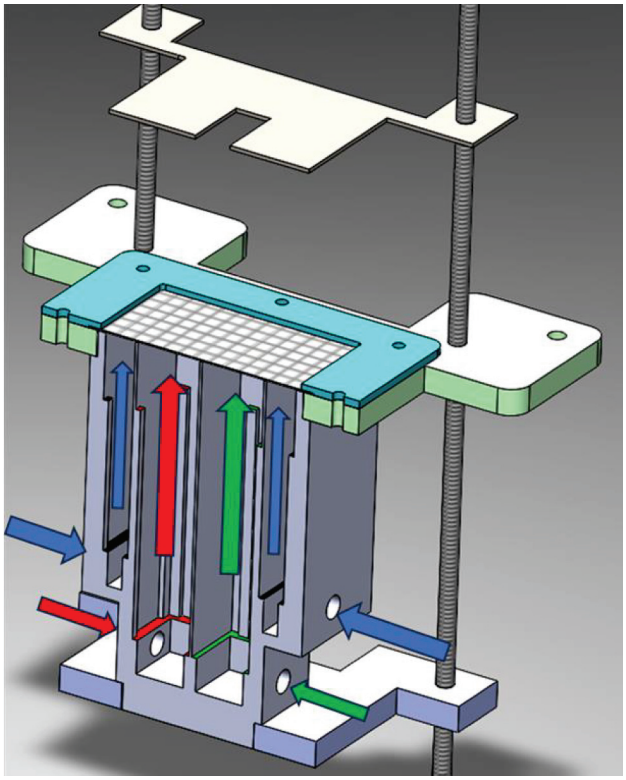

Fig. 1. Cross-section of the PMLF burner with arrows showing the streams of fuel (red), oxidizer (green), and shielding nitrogen (blue).

X_{FF}=0.260 and X_{OO} =0.179, respectively. These boundary conditions establish a PMLF with a visually mild soot load (i.e., volume fraction of the order of 10^{-8}) which is compatible with capillary sampling. To achieve the best flow stability with the selected boundary conditions, the optimal width of the exhaust slit in the stabilization plate is set to 14 mm with an off-axis displacement of 2 mm toward the oxidizer stream of its center relative to the splitter of the reactant nozzles.

Digital imaging is performed to track the flame stability and the positioning of the measurement probes. Images are acquired with a resolution of approximately 15 μm/pixel using a Nikon D750 digital camera equipped with a Nikkor $F = 85$ mm/1.4 prime lens coupled to an achromatic close-up lens (sigma, AML72-01) with an angle of view parallel to the splitter of the reactant nozzles. The lens is F-stopped either at 8 to establish a deep field across the whole PMLF to check its stability or at 2 for sharp probe positioning when acquiring images (or videos). In each case, more than 50 images are captured at 1 Hz for subsequent analysis. The great stability of the PMLF without and with sampling is also documented by recording Videos S1 and S2-S3 of the Supplementary Materials (SM), respectively. Specifically, Video S2 shows the PMLF during the capillary sampling used in this study. Instead, Video S3 is recorded while sampling the PMLF with a horizontal tube dilution probe of the type used for soot size distribution measurements [73] but the results of applying this technique are not discussed herein. Sections 2.2-2.4 below detail the techniques used to characterize the investigated PMLF and a schematic of the whole experimental setup is included in Fig. S1 of SM. A list of nomenclature used throughout this manuscript is also included in section SM1 of SM.

2.2. Capillary sampling for quantitative GG/MS analyses

Capillary sampling has been used successfully in the literature to resolve the structure of very thin CFs [32,36,48–56,74,75]. In this work, a fused silica capillary (ID/OD= 0.20/0.31 mm) whose outlet is kept under vacuum (i.e., increasing from 0 to 300 torr during sampling), is

inserted in the PMLF at the desired HAB parallel to the splitter of the reactant nozzles and the PMLF luminous layers to sample the gas from a thin flame layer with nearly constant Temperature (T) and composition [15]. The probe is pre-positioned at the desired HAB by moving the burner with a vertical translation stage. Capillary sampling is performed from different layers of the PMLF upon repositioning the burner assembly relative to the fixed probe with a horizontal translational stage. The horizontal distance between the capillary probe tip and the blue chemiluminescence ($\overline{\overline{x}}$) is measured by processing in Matlab more than 50 digital images sharply focused on the capillary tip which are acquired during each sampling, as further detailed in Fig. S2 of the SM. All experimental results are presented with horizontal error bars of $\overline{\overline{x}}$ bracketing its 95 % confidence interval [76].

The flame samples are stored for less than 30 s at 300 torr and 473 K before being injected in a custom configured Gas Chromatograph/Mass Spectrometer (GC/MS). The path from the capillary probe to the storing volume and GC injection ports is also kept at 473 K to avoid condensation of heavy species. The GC/MS is configured to perform quantitative measurements of more than forty-five i-species whose mole fraction (X_i) is as low as ≈10 ppb. The sample components are separated, in most cases with the desirable isomeric resolution, by four GC columns and quantified by three detectors whose responses are calibrated using internal calibration standards [32,48–51]. The Thermal Conductivity Detector (TCD) chromatogram is used to quantify N_2, O_2, H_2O, CO, CH_4, C_2H_4, and H_2. The chromatogram measured by the Flame Ionization Detector (FID) installed downstream of a methanizer quantifies CO, CO_2, and (oxygenated) hydrocarbon species as light as CH_4 and composed of up to 7 carbon atoms (i.e., toluene). Repetitions of the TCD and FID response calibrations and flame measurements of X_i have an uncertainty smaller than ±2.5 % with a 68 % confidence [76]. The chromatogram generated by MS quantifies (oxygenated) hydrocarbons composed of at least 4 carbon atoms and as heavy as cyclopenta[cd]pyrene and its isomers, including a broad variety of Policyciclic Aromatic Hydrocarbons (PAHs) that may be involved in soot inception. Repetitions of the MS response calibrations and flame measurements of X_i have an uncertainty smaller than ±10 % and ±15 % with a 68 % confidence [76], for species as heavy and heavier than naphthalene, respectively.

2.3. Fine thermocouple measurements

Measurements of T are necessary given its strong influence on all chemical and soot kinetics [10]. They are performed at HAB= 50 mm using a silica-coated cylindrical R-type thermocouple (TC) with a junction diameter d_{bead}=137 μm. The TC wires are inserted parallel to the fuel/oxidizer splitter with the junction positioned in the middle of the nozzles. A 60 mm wide holder establishes TC pre-tensioning to compensate for thermal expansion [75,77,78] and minimize any junction positioning unsteadiness. The TC junction is sharply focused in the more than 50 digital images acquired to track the measurement $\overline{\overline{x}}$, with the same procedure as during capillary sampling. The results are presented with horizontal error bars of $\overline{\overline{x}}$ bracketing its 95 % confidence interval [76]. Measurements are corrected for radiation heat losses with the method detailed in section SM2 of the SM and results are presented with vertical error bars bracketing their 68 % confidence interval [76].

2.4. Computational modeling

Two-dimensional Computational Fluid Dynamics (2D-CFD) modeling is implemented using the Fluent Ansys software package and two detailed chemical kinetic models, namely USC [79] and a slightly modified version [80] of ABF [19]. USC is one of the most robust models detailing oxidation and oxidative pyrolysis of C1-C4 hydrocarbons over a broad range of stoichiometries whereas ABF is comparatively less detailed for C1-C4 but accounts for the formation of PAHs as heavy as pyrene which may be involved in soot formation [18–20,30]. The modification [80] of ABF involves only two recombination reactions forming phenanthrene (A3) isomers (i.e., phenylacetylene with either phenyl or benzene) and consists of zeroing the temperature exponent and reducing the original [19] pre-exponential factors and activation energies of 53 % and 16 %, respectively. In the investigated conditions, the modification affects only species composed of three or more aromatic rings causing a reduction of their predicted X_i smaller than 10 %.

2D-CFD accounts for buoyancy and mixture-averaged diffusion transport, including thermal diffusion (i.e., Soret effect) [81]. Heat losses by gas radiation are computed under the assumption of an optically thin medium by implementing an Ansys Fluent external function to calculate the spectrally averaged emissivities of CO_2, CH_4, CO, and H_2O as a function of the local T using dedicated polynomial fittings [82,83]. Fig. 2 depicts a mesh of the 2D-CFD computational domain in which the $\overline{x}$ axis is the horizontal distance from the splitter separating the fuel nozzle on the left at $\overline{x}$<0 from the oxidizer nozzle to the right at $\overline{x}$>0. The inflow and outflow boundary conditions are highlighted in the figure using inward-pointing blue and outward-pointing red arrows, respectively. Plug flows with V_F= V_{Ox}= V_{N2}= 0.20 m/s are assigned to both the fuel, oxidizer, and shielding nitrogen inlets whereas a (near atmospheric) Bernoulli distribution of p is assigned to the outlets. Adiabatic nonslip boundary conditions are assigned to the rest of the boundary (green without arrows) which correspond to the surface of the slotted stabilization plate.

The Ansys Fluent adaptive mesh refinement is utilized within each cell where the percentage changes (relative to the cell average) of the values (G) and values of the gradients (C) of T, velocity magnitude, and X_is of C_2H_4, O_2, and benzene (A1) are larger than selected thresholds. Refined results are obtained by setting progressively smaller thresholds, from 5 % to 0.5 % and from 10 % to 1 % for G and C, respectively. Mesh-independent T and X_{A1} fields with both USC and ABF are computed when G ≤ 1 % and C ≤ 2 % (see Fig. S3 in SM). Fig. 2 shows the refined mesh satisfying these conditions with USC whose mesh-independent results predict T_{max} in the PMLF horizontal cross-sections at HAB= 25 mm and 50 mm to be 1786 K and 1776 K, respectively. The lowering of

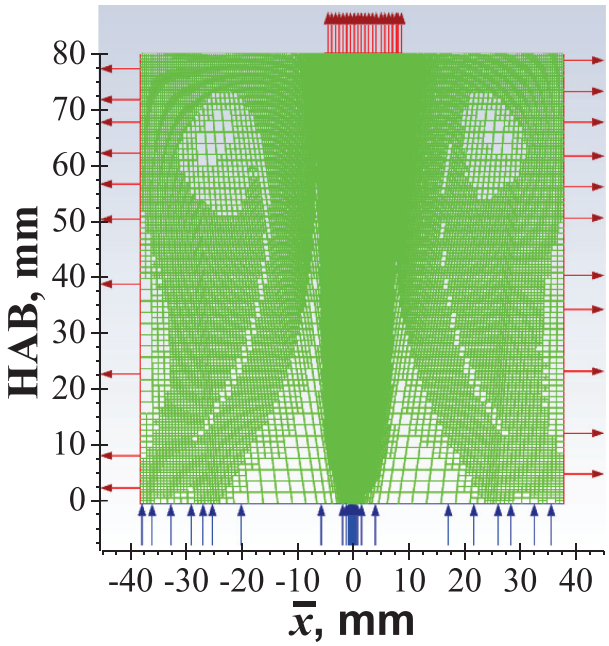

Fig. 2. Refined computation mesh used for 2D-CFD with USC [79]. The blue inward arrows highlight the plug flow inlets of fuel, oxidizer, and shielding nitrogen whereas the red outward arrows indicate outlets with a near atmospheric Bernoulli pressure distribution. Adiabatic non-slip conditions are assigned at the plate surface which is the top green boundary without arrows.

T_{max} at increasing HABs is caused by radiation heat losses to which soot is estimated to contribute [84] negligibly compared to the computed gas heat losses, as documented in the literature for several CFs with Z_{st}=0.183 and soot volume fractions at least as large as 10^{-7} [52,53].

One-dimensional CF modeling (1D-CF) is performed with the planar solver of Ansys Chemkin Pro using either USC [79] or the modified ABF [19,80] and accounting for mixture-averaged diffusion transport, including thermal diffusion (Soret effect), as in 2D-CFD. Plug flow boundary conditions with equal velocities for the fuel and oxidizer counterflowing streams, $u_F = u_{Ox} = a \bullet L/2$, are used. A large 80 mm nozzle separation distance (L) is selected to minimize CF confinement effects on the field of local strain rate (a'). The global strain rate (a) value is selected as in CFs characterized in the literature [e.g.,32,50–52] or to obtain a T profile with the same thickness as the characterized horizontal cross-section of the PMLF. As detailed in the results section, a 1D-CF with the same Z_{st}, T_{max}, and (T profile) thickness of the selected PMLF horizontal cross-section mimics its entire thermochemical structure, including diffusion and advection transport. Therefore, the PMLF horizontal profiles can be modeled approximately as an equivalent 1D-CF using any, even extremely detailed, chemical kinetic model at a fraction of the 2D-CFD computational cost.

3. Results and discussion

3.1. Boundary layer structure of the Planar Mixing Layer Flame (PMLF)

The left panel of Fig. 3 shows a typical digital image of the investigated PMLF with an angle of view parallel to its luminous layers. The blue chemiluminescence overlaps with the oxidation layer [85–87] whereas the adjacent orange luminosity is an incandescent soot layer growing thicker at increasing HABs. The thickening continues until the flow accelerates near the slotted cold stabilization plate which distorts the PMLF structure at HAB> 65 mm. Digital imaging guides the identification of the operating conditions to achieve the desired PMLF stability, horizontal thickness, and slight sooting loads compatible with implementing intrusive sampling with the desired spatial resolution. The flow stability is assessed by tracking the horizontal displacement of the flame blue chemiluminescent layer which fluctuates horizontally less than a twentieth of the horizontal thickness of the orange luminous zone of the flame at all investigated HABs.

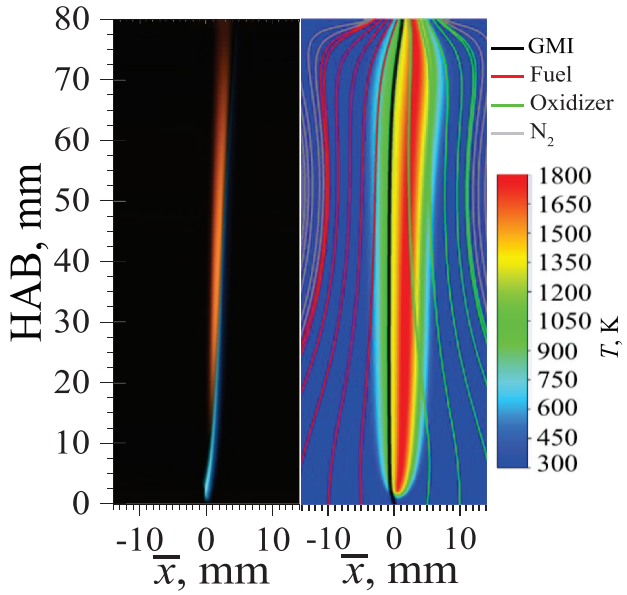

Fig. 3. Overall structure of the investigated nitrogen-diluted PMLF fueled by ethylene with Z_{st}=0.183, X_{FF}=0.26, and 0.2 m/s velocity at the nozzle outlets. The digital image of the PMLF in the left panel highlights the blue chemiluminescence of the oxidation layer and the orange luminosity of soot. The right panel shows the results of 2D-CFD with the temperature (T) field superimposed to (colored) gas streamlines including the Gas Mixing Interface (GMI, in black) which separates the fuel streamlines (in red) to its left from the oxidizer streamlines (in green) to its right, all being sandwiched between the streamlines of the shielding nitrogen (in gray). The abscissa is the horizontal distance ($\bar{x}$) from the fuel and oxidizer splitter.

Indeed, the horizontal position of the maximum blue chemiluminescence fluctuates with a standard deviation smaller than 0.10 mm and 0.15 mm at HAB=25 mm and 50 mm where the thickness of the orange sooting luminous zone is approximately 2.3 and 2.9 mm, respectively. The flow stability of the investigated PMLF is further highlighted in Videos S1-S3 included in the SM. The negligible fluctuation and large thickness in a planar geometry make the PMLF ideal for obtaining experimental results with good spatial resolution even when using intrusive sampling.

The right panel of Fig. 3 depicts the results of 2D-CFD with the gas streamlines originating from the fuel (in red to the left) and oxidizer (in green to the right) nozzles sandwiched between the gas streamlines of the shielding nitrogen (in gray on both sides), being superimposed on the color-coded Temperature (T) field. The comparison of the left and right panels of Fig. 3 highlights that the positions of the T maxima (T_{max}) in the horizontal cross-sections of the PMLF lie within the oxidizer stream and overlap with the blue chemiluminescence maxima. Indeed, the heat release rate and CH* peak at the same locations in most hydrocarbon-fueled flames [85–87]. At increasing HABs, the T_{max} and blue chemiluminescence experience a progressive displacement to the right away from the fuel and oxidizer splitter at $\bar{x}$= 0 mm and the Gas Mixing Interface (GMI). The GMI is the gas streamline separating the fuel and oxidizer streams and is shown in black at the center of the right panel of Fig. 3. The position of T_{max} to the right of the GMI is consistent with the selection of Z_{st}=0.183<0.5 which causes the stoichiometric mixing necessary for the main oxidation reactions to be established in the oxidizer stream [16]. The displacement away from the GMI indicates that the flame experiences decreasing strain rates at increasing HABs, consistent with the decrease in scalar dissipation rates observed by Norton et al. in a modified Wolfhard-Parker planar co-flow flame [37]. The comparison of 2D-CFD and experimental results in Fig. 3 reveals also that the faint soot-orange luminosity observed in the image is mostly sandwiched between the blue oxidation layer and the GMI. In the right panel of Fig. 3 an exemplar green gas streamline originating from the cold oxidizer nozzle at $\bar{x}$= 5 mm crosses T_{max} before entering the soot-laden region and approaching asymptotically the GMI. This means that soot particles nucleate and age as the flame products are transported by advection away from the oxidation layer toward the colder and carbon-richer GMI and possibly beyond it by thermal and Brownian diffusion. It appears that the advection histories leading to soot formation in the PMLF are very similar to that established in CFs with the same Z_{st}=0.183 where soot formation occurs while the flame products are advected from T_{max} toward the Gas Stagnation Plane (GSP) separating the fuel and oxidizer streams [36,88]. In brief, there are substantial similarities between a PMLF and a CF with the same Z_{st} but the advection histories along different gas streamlines of each reactant are slightly polydisperse in the PMLF, as further detailed in Section 3.4, whereas they are monodisperse in a 1D-CF [49–51].

Before diving into the detailed comparison of a PMLF and CFs with the same Z_{st} in ensuing sections, it is worth providing some additional insight into the overall boundary layer structure of the PMLF. Fig. 4 depicts the PMLF horizontal thermal thickness (δ_T) which is two times the FWHM of the horizontal profiles of the reduced temperature (Θ=[T-T_{min}]/[T_{max}-T_{min}]) [57] field computed by 2D-CFD, validated by T measurements at HAB= 50 mm. Fig. 4 includes also the horizontal thickness of the orange sooting luminosity (δ_{soot}) with the shaded area bracketing the standard deviation of the results obtained by processing 100 images of the PMLF. The values of δ_{soot} are quantified as two times the FWHM of the horizontal profile of the reduced [57] red channel

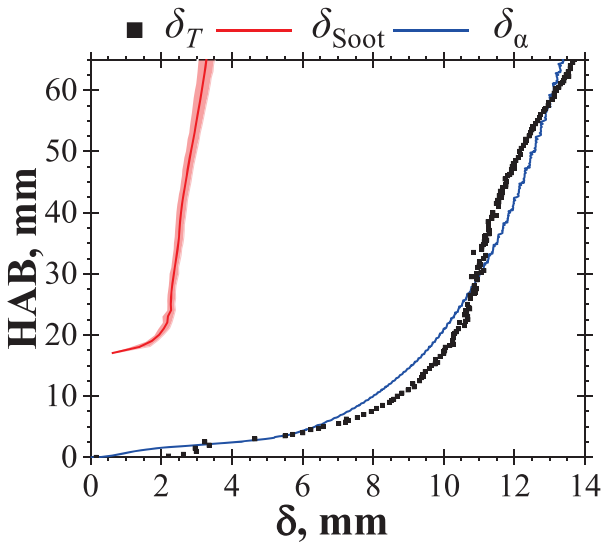

Fig. 4. PMLF horizontal thicknesses (twice the FWHM) at different HABs of the reduced T (i.e., Θ) computed by 2D-CFD (δ_T) and the luminous sooting layer measured in digital images (δ_{soot}), compared to the estimated thickness of a thermal boundary layer (δ_α) growing as a result of thermal diffusion due to the heat of reactions being released in a thin layer in the proximity of the GMI.

counts at all HABs but at HAB ≤ 22 mm where such value is reduced of the FWHM of the reduced blue channel counts profile to compensate for the fact the blue chemiluminescence dominate over the soot luminosity at those low HABs.

The profiles of δ_T and δ_{soot} as a function of HAB are compared to that of the estimated thickness ($\delta_\alpha = 3.6\cdot\sqrt{\alpha_{GMI}\cdot t_{GMI}}$) [57] of a thermal boundary layer growing during the advection time (t_{GMI}) along the GMI, necessary for the flow to reach different HABs after exiting either of the reactant nozzles. The estimate is based on the local value of the thermal diffusivity (α_{GMI}) along the GMI at each t_{GMI}-HAB which is calculated as the integral along the GMI of the inverse of the velocity magnitude. A very similar shape of the δ_α profile in Fig. 4 is obtained if the advection time and the thermal diffusivity are estimated along any other streamline originating from either the fuel or the oxidizer nozzle. It is also noteworthy to mention that profiles with the same shape as that of δ_α are obtained also by estimating the thickness of the mixing boundary layer of any i-species (δ_{Di}) by replacing α_{GMI} with its molecular diffusivity ($D_{i,GMI}$) along the GMI or any other streamline. The overlapping of δ_T and δ_α in Fig. 4 highlights that the PMLF has a boundary layer structure from the diffusion transport point of view, as further detailed in the ensuing Sections 3.2-3.3. Also, Fig. 4 highlights that the similarity may apply to soot as well, given that δ_{soot} is approximately a quarter of δ_T at any HABs≥22 mm. Importantly, the horizontal cross-sections of the PMLF are much thicker compared to CFs which can be stabilized and characterized reliably in experiments. For example, δ_{soot} is 2.9 mm at HAB= 50 mm which is approximately three times thicker than the sooting zone of CFs with Z_{st}=0.183 and a = 52.6 /s investigated in the literature [32,36,50–56]. Last but not least, the structure of a PMLF horizontal cross-section is minimally influenced by any downstream perturbation. This is due to the co-flow nature of the PMLF and the governing equation of any boundary layer being mathematically parabolic. These characteristics make the PMLF amenable to achieving the desired spatial resolution using intrusive sampling, including the dilution probes (see Videos S3 and [89]) used routinely to measure the soot size distribution function in burner-stabilized premixed flames [58–60]. As an additional benefit, the PMLF enables the investigation of chemical kinetics on relatively long time scales ($\tau \cong HAB/\sqrt{2g\cdot HAB\cdot[1-T_{min}/T_{max}]}$) of the order of tens of milliseconds that are directly relevant to combustion applications. Therefore, all the experimental datasets generated in PMLFs will be valuable in validating chemical kinetic models in application-relevant conditions that cannot be investigated in 1D-CF experiments.

3.2. Thermochemical self-similarity of the PMLF and its equivalent 1D-CFs

Fig. 5 depicts the boundary layer self-similar structure of the horizontal cross-sections of the PMLF and compares it to the computed structure of a few planar 1D-CFs with the same Z_{st}=0.183. The figure includes the profiles of the reduced T (i.e., Θ=[T-T_{min}]/[T_{max}-T_{min}]) and mole fractions (i.e., Ξ_i=[X_i - $X_{i,min}$]/[$X_{i,max}$- $X_{i,min}$]) of C0-C2 species [57], including the reactants, as well as that of benzene (A1) which is an important intermediate to soot formation [20]. The solid and dotted lines show the horizontal profiles computed by 2D-CFD with USC at HAB= 50 mm and 25 mm, respectively. Also, the solid and hollow symbols depict the experimental results at HAB= 50 mm and 25 mm, respectively. 1D-CF results with USC (dashed lines) are computed for planar 1D-CFs with Z_{st}=0.183 and are practically indistinguishable for computations performed reducing a from 52.6 /s, as in literature axisymmetric CFs [32,36,50–56], down to 7.0 /s, as in a 1D-CF with the same thickness of the horizontal cross-section of the PMLF (δ_T in Fig. 4) at HAB= 50 mm. Almost identical computational results are obtained by using ABF rather than USC, as shown in Fig. S4 of the SM, or an axisymmetric rather than a planar 1D-CF solver.

The distance (x) in the abscissa of Fig. 5 is divided by the δ_T of the considered case (see legend) and measured horizontally from the GMI in the PMLF ($x = \bar{\bar{x}} - \bar{\bar{x}}_{GMI}$@HAB) and from the GSP in 1D-CFs, being negative and positive in the fuel and oxidizer streams, respectively. The GMI position ($\bar{\bar{x}}_{GMI}$@HAB) is obtained from the 2D-CFD results by assuming the horizontal maxima of the blue chemiluminescence to coincide with that of the heat release rate and CH* [85–87]. The PMLF horizontal cross sections (and their equivalent 1D-CFs) have δ_T = 10.3 mm and 12.0 mm in the PMLF at HAB= 25 mm (1D-CF with a = 9.8 /s) and 50 mm (a = 7.0 /s), respectively (see also Fig. 3). 1D-CF with a = 52.6 /s, also considered in Fig. 5, has δ_T = 4.50 mm.

In Fig. 5, the non-dimensionalization of x using the δ_T (thermal) diffusion length and the ordinate by reducing [57] T and X_is highlights the self-similarity of the flame structures. Each profile in Fig. 5 is the same in different PMLF horizontal cross-sections as in 1D-CFs with the same Z_{st}=0.183. The shape of the profiles is determined exclusively by the spatial distribution of the (normalized) production rate of the considered i-species (heat release rate for Θ) in addition to that of its molecular (thermal for Θ) diffusivity. The agreement between computational and experimental results in Fig. 5 demonstrates not only that the models can predict accurately the aforementioned spatial distributions for the heat release rate and production rate of C0-C2 species and benzene but also that capillary sampling spatially resolves the structure of the investigated PMLF horizontal cross sections. One may notice only a slight variation in the boundary condition of C_2H_6 which is present as an impurity at the hundreds of ppm level in the used ethylene bottle. Such experimental deviation is not significant and is caused by the level of the C_2H_6 impurities changing for repetitions of the experiments on different days as the bottle content stratifies. Fig. 5 demonstrates that the PMLF horizontal cross-sections have a flamelet structure equivalent to that of 1D-CFs with the same Z_{st}, the most significant difference being that the maximum δ_T achievable in 1D-CF experiments is strictly limited by the onset of buoyant instabilities and 2D flow distortions as one reduces a [47,65]. Therefore, it is not possible to stabilize and investigate experimentally a quasi-1D CF with arbitrarily low values of a and correspondingly large δ_T as in the PMLF. Nonetheless, experimentally inaccessible 1D-CFs can be modeled to find what value of a makes the δ_T of a CF the same as that of a designated horizontal cross-section of the PMLF.

For the sake of completeness and ensuing quantitative comparisons,

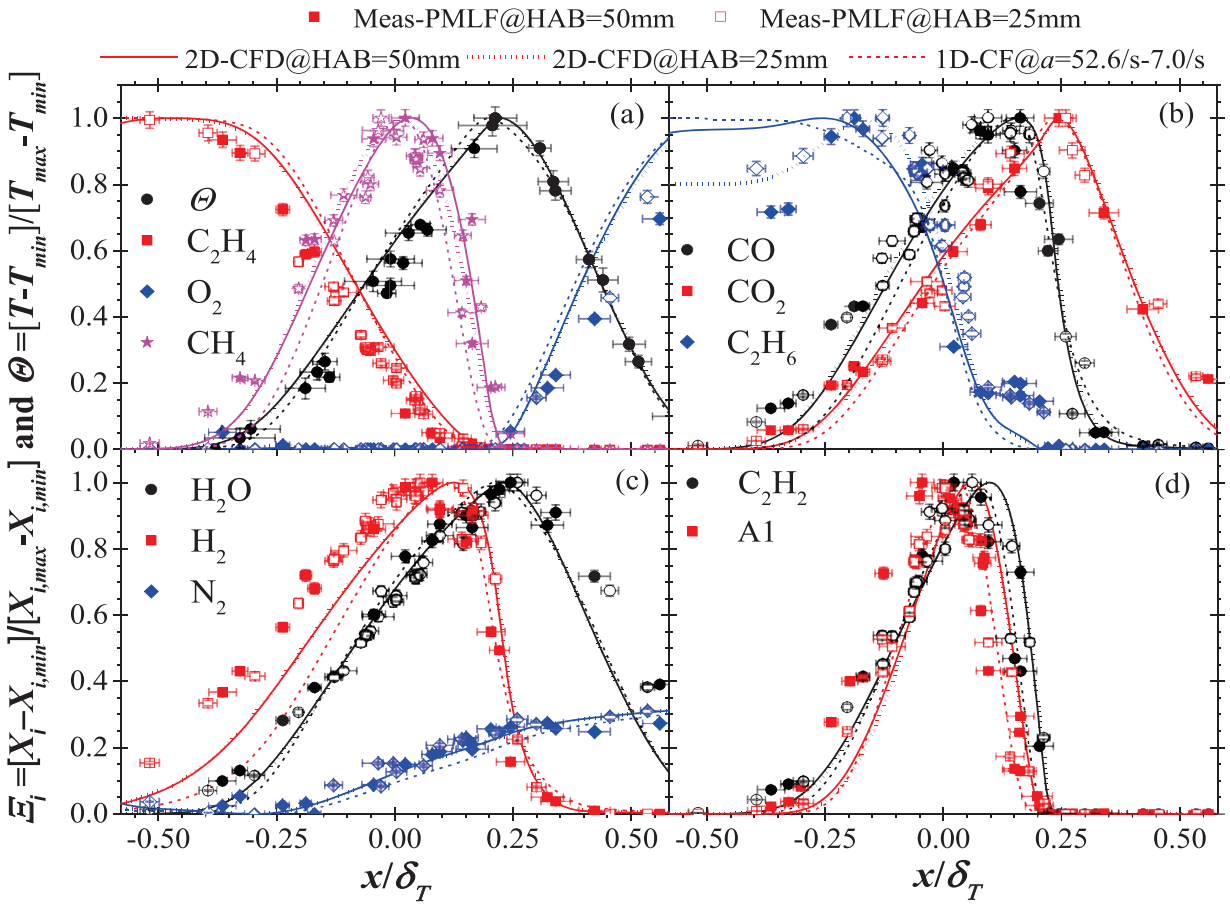

Fig. 5. Self-similar profiles of reduced a) temperature (Θ) and mole fraction (Ξ_i) of a) ethylene, methane, and oxygen; b) ethane, CO, and CO_2; c) H_2, N_2, and H_2O; and d) benzene (A1) and acetylene. Measurements and computations with USC [79] are shown as a function of the distance (x), scaled over the thickness (δ_T) of the Θ profile, from the GMI and the GSP in the PMLF and CFs, respectively. Results consider the PMLF at HAB= 25 mm and 50 mm and planar 1D-CFs with the same Z_{st}=0.183 and any a from 7.0 /s to 52.6 /s.

the values of T_{max}, T_{min}, $X_{i,max}$, and $X_{i,min}$ used to reduce the profiles in Fig. 5 (and Fig. S4) are listed in Table 1 for both experimental and USC and ABF modeling results. Also, the non-reduced T and X_i profiles are shown in Figs. S5-S6 of SM. Fig. 5 and Table 1 (and Fig. S5) provide a validation of the capability of 2D-CFD to predict accurately the PMLF T field. Such validation is highlighted by an excellent agreement between the thermocouple measurement and the model results over most of the horizontal span of the PMLF at HAB= 50 mm which is the highest investigated HAB. Indeed, one expects the model to have increasingly less accurate predictive performances at increasing HABs due to error compounding in solving the approximately parabolic governing balance equation. This is the case even though ANSYS solves the fully coupled elliptic governing equations.

Table 1 includes the results for 1D-CFs with a = 9.8 /s and 7.0 /s whose Z_{st}, δ_T, and T_{max} are equal to that of the PMLF horizontal cross-sections at HAB=25 mm and HAB=50 mm, respectively. It appears that these properly selected equivalent 1D-CFs can mimic not only the shape of the profiles of Fig. 5, but also $X_{i,max}$ and, therefore, the absolute

Table 1
Mole fraction maxima ($X_{i,max}$) used for reducing the self-similar profiles of Fig. 5 which depict the structure of several nitrogen-diluted planar non-premixed *flamelets* fueled by ethylene with Z_{st}=0.183 and with reactants temperature T_{min}=298 K. Note $X_{N2,max}$=1 and $X_{i,min}$=0 for all species but $X_{N2,min}$=1- X_{FF}.

Flame profile	T_{max}, K	X_{FF}	X_{oo}	$X_{i,max}$							
		C_2H_4, %	O_2, %	H_2, %	CH_4, %	H_2O, %	CO, %	CO_2, %	C_2H_2, %	C_2H_6, ppm	A1, ppm
Meas-PMLF@HAB=50mm	**1793**	**26.0**	**17.9**	**1.40**	**0.10**	**8.75**	**3.23**	**8.27**	**1.33**	**98**	**138**
2D-CFD-USC@HAB=50mm	1776	26.0	17.9	1.12	0.13	8.76	3.23	8.09	1.16	168	48
1D-CF-USC@a=7.0/s	1776	27.2	18.7	1.10	0.10	8.87	3.36	8.78	1.14	169	51
2D-CFD-ABF@HAB=50mm	1782	26.0	17.9	1.73	0.09	9.28	3.50	7.78	2.07	180	105
1D-CF-ABF@=7.0/s	1782	27.6	19.0	1.66	0.06	9.37	3.71	8.61	2.05	172	66
Meas-PMLF@HAB=25mm	-	**26.0**	**17.9**	**1.57**	**0.14**	**8.86**	**3.38**	**7.99**	**1.38**	**150**	**134**
2D-CFD-USC@HAB=25mm	1786	26.0	17.9	1.16	0.17	8.77	3.41	7.98	1.14	202	41
1D-CF-USC@=9.8/s	1786	27.0	18.6	1.15	0.11	8.76	3.53	8.57	1.16	168	45
2D-CFD-ABF@HAB=25mm	1803	26.0	17.9	1.81	0.13	9.28	3.73	7.76	2.06	241	138
1D-CF-ABF@=9.8/s	1803	27.8	19.2	1.80	0.06	9.42	4.00	8.47	2.18	173	70
Meas-CF@=52.6/s [50]	**1989**	**33.0**	**22.9**	**3.29**	**0.13**	-	**5.44**	**9.39**	**2.51**	**93**	**137**
1D-CF-USC@=52.6/s	2006	33.0	22.9	2.18	0.19	10.5	6.54	8.91	1.85	206	54.5
1D-CF-ABF@=52.6/s	1980	33.0	22.9	3.10	0.10	11.0	6.77	8.55	3.37	206	110

production rates of C0-C2 species. To select the equivalent 1D-CF, a and $X_{C2H4.max}$ in the fuel stream (X_{FF}) have to be tuned for the 1D-CF to match δ_T and T_{max} of the selected PMLF horizontal cross-section, respectively. Therefore, one may notice that the nitrogen dilution of the equivalent 1D-CF has to be slightly perturbed compared to the PMLF boundary conditions to match the target T_{max}. The perturbation is necessary because of unavoidable 2D effects and since, according to 2D-CFD and 1D-CF results, radiation heat losses are relatively less significant in the PMLF compared to the equivalent 1D-CF. The change in the boundary conditions consists of a minimal increase of X_{FF} and $X_{O2,max}$ in the oxidizer stream (X_{OO}), consistent with keeping Z_{st}=0.183. Table 1 lists the values of X_{FF} and X_{OO} set for 1D-CFs to have the same T_{max} as the PMLF at HAB 25 mm and 50 mm, respectively. One can rescale the 1D-CF results by multiplying the computed X_is by the ratio $X_{FF\text{-}CF}/X_{FF\text{-}PMLF}$ which is equal to 1.038 and 1.046 for USC (1.067 and 1.061 for ABF) to account for the slightly different carbon flux in the equivalent 1D-CFs compared to that in the PMLF at HAB= 25 mm and 50 mm, respectively. Even upon considering such a small correction, Table 1 demonstrates that the equivalent 1D-CFs predict the experimental horizontal profiles of C0-C2 species in the PMLF with the same accuracy as 2D-CFD using either USC or ABF. The only exception is that 2D-CFD predicts roughly twofold more benzene than 1D-CF with ABF. As for other small inaccuracies of tested chemical kinetic models in reproducing the experimental results, USC underpredicts hydrogen noticeably, acetylene slightly, and benzene approximately threefold whereas ABF overpredicts both hydrogen and acetylene noticeably but is somewhat more accurate than USC in predicting benzene in 2D-CFD.

All C0-C2 combustion products are relatively well predicted by both USC and ABF which is the result of the robust existing knowledge of the kinetic parameters for the main oxidation reactions of C1-C4 hydrocarbons as an outcome of decades of studies of laminar flames [e.g.,90, 91]. Given this fact, Fig. 6 depicts the profiles of some major and minor radicals and hydrogen peroxide in the PMLF at HAB= 25 mm and 50 mm computed by 2D-CFD and equivalent 1D-CF with USC [79]. The abscissa of Fig. 6 is the same as in Fig. 5 to highlight to what extent the self-similarity applies also to the profiles of radicals involved in the flame oxidation and pyrolysis chemistry. Indeed, the predictions of 2D-CFD and equivalent 1D-CF are virtually indistinguishable from each other in the oxidizer stream at $x > 0$. Specifically, the profiles of H, O, and OH show that these important radicals are mainly produced in the oxidation layer of the flame at $x/\delta_T > 0.20$ near but to the right of T_{max} which is at $x/\delta_T \approx 0.20$. On the other hand, the profiles of propargyl radical (C_3H_3) and other hydrocarbon radicals not shown in the figure also peak near T_{max} but lean toward the carbon-richer zone of the flame at Ts exceeding 1000 K in the region where $-0.05 < x/\delta_T < 0.20$. Lastly, oxygenated species formed at both high and low Ts, such as hydrogen peroxide (H_2O_2) and hydroperoxyl radical (HO_2), have double-peaked profiles with one peak in the oxidizer stream $x/\delta_T > 0.30$ which is the same in 1D-CF and 2D-CFD and another peak at $x/\delta_T < -0.10$ in the fuel stream which is predicted only by 2D-CFD. The H_2O_2 and HO_2 peaks at $x/\delta_T < -0.10$ are more pronounced at HAB=25 mm compared to HAB=50 mm and are due to advective leakage of flame intermediates generated in the PMLF leading edge at low HABs $\leq$ 5 mm.

In summary, Fig. 6 broadens the applicability of the equivalent 1D-CF to radical species but shows that 2D effects may modify the self-similar profiles of some species in the cold ($T < 1000$ K) fuel pyrolysis region ($x < -0.05$) of the flame. One type of 2D effect is due to the advective leakage of flame intermediates from the PMLF leading edge at low HABs which cannot be accounted for in the equivalent 1D-CF. Fortunately, the X_is of the leaked H_2O_2 and HO_2 are too low (about 10 ppm) to affect substantially the PMLF structure at either HAB= 25 mm or 50 mm.

3.3. Self-similar profiles of C3-C18 species in the PMLF and equivalent 1D-CFs

One would wonder if the equivalent 1D-CFs with the same Z_{st}, δ_T, and T_{max} as the investigated PMLF horizontal cross-sections can predict the profiles (i.e., diffusivity and the relative spatial distribution of the production rate) of minor flame products, including Policyciclic Aromatic Hydrocarbons (PAHs) which are important in soot inception, as well as their $X_{i,\max}$ (i.e., absolute values of their production rates). To investigate this aspect and compound the data in Figs. 5-6 and Table 1, Figs. 7-8 show the X_i profiles of C3-C18 species measured in the PMLF at HAB= 25 mm and 50 mm with hollow and solid symbols, respectively. Figs. 7-8 include the results of 2D-CFD and equivalent 1D-CF depicted with solid and dash-dotted lines, respectively. All profiles are plotted as a function of the distance (x) from the GMI in the PMLF cross-sections or the GSP in 1D-CFs, still with $x < 0$ and $x > 0$ being in the fuel and oxidizer streams, respectively.

To begin with, Fig. 7 shows the profiles of C3-C7 species as heavy as toluene, most of which are relatively well predicted only by USC which is the only chemical model considered in the figure. ABF is somewhat less effective compared to USC in predicting most C3-C5 species and the comparison of its predictions with the experimental results is relegated to Fig. S7 of the SM. An aspect to notice in Fig. 7 is that for certain species, primarily formaldehyde (CH_2O) and C_3H_8 and, to a much lesser extent, propyne (p-C_3H_4), C_3H_6, C_4H_8, and c-C_5H_6, 2D-CFD predicts noticeably larger X_is for $x < 0$ and better captures the shape of the experimental profiles compared to 1D-CF. This difference is likely due to the 2D leakage discussed in Fig. 6 for H_2O_2 and HO_2. The shape of the profiles predicted by 2D-CFD and equivalent 1D-CFs are virtually indistinguishable or at least very close to each other for all other species, including allene (a-C_3H_4). USC in 2D-CFD reproduces extremely well the measurements of p-C_3H_4, C_3H_6, CH_2O (both at $x < 0$ and $x > 0$), C_3H_8, and C_4H_6 whereas it overpredicts, roughly by a factor of two, X_is of C_4H_2

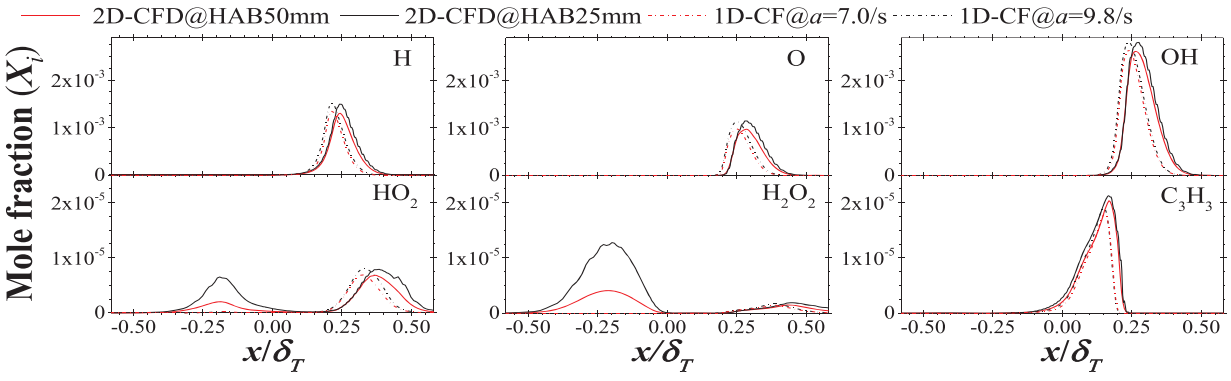

Fig. 6. Profiles of major radicals, HO_2, H_2O_2, and C_3H_3 in the PMLF at HAB= 25 mm and 50 mm as computed by 2D-CFD (solid lines) and equivalent 1D-CF (dashed lines) with USC [79]. The distance (x) from the GMI of the PMLF and GSP of CFs in the x-axis is scaled over δ_T, as in Fig. 5.

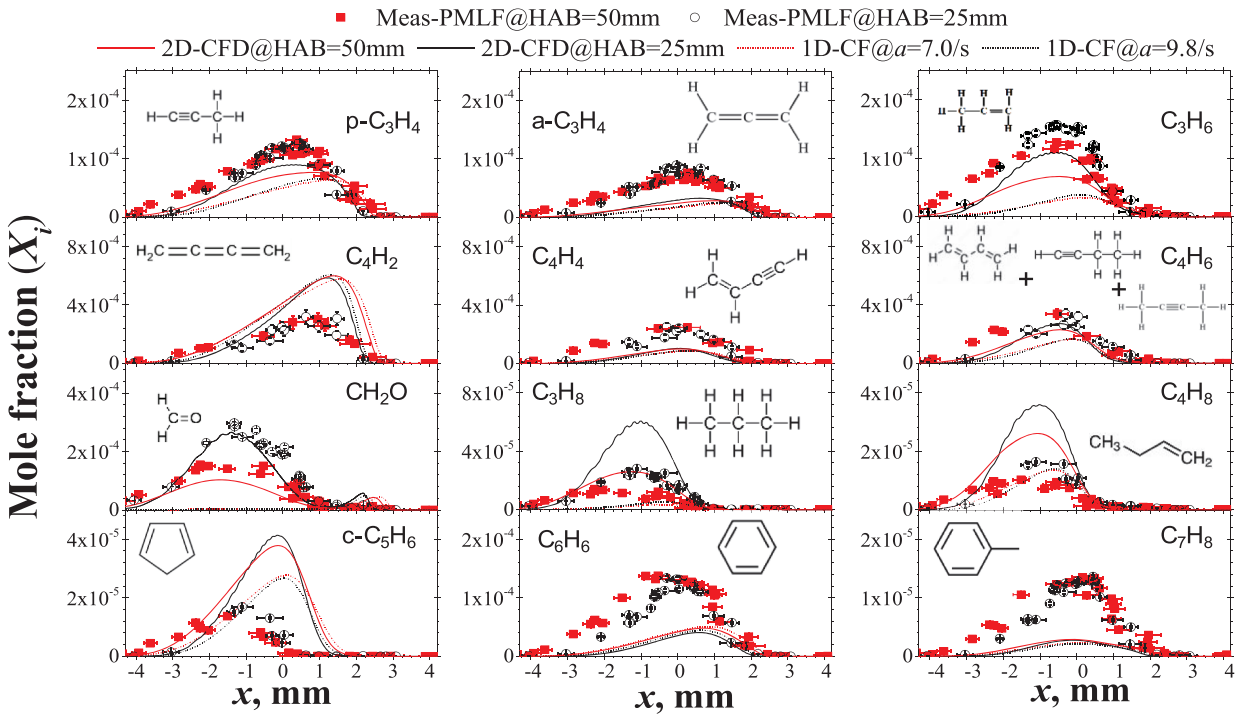

Fig. 7. Measured and computed profiles of C3-C7 species at HAB= 25 mm and HAB= 50 mm. Computations are performed by 2D-CFD and equivalent 1D-CFs with USC [79]. The abscissa is the distance (x) from the GMI in the PMLF cross-sections or the GSP in the equivalent 1D-CFs.

and C_4H_8. On the other hand, USC underpredicts roughly by a two-factor some species important in the formation of the first aromatic ring such as a-C_3H_4, C_3H_6, and C_4H_4. The large underestimation of A1 and toluene (roughly three- and five-fold, respectively) can be attributed only in part to the underestimation of these C3-C4 species. It is noteworthy to mention that the USC predictions of A1 in the ethylene-fueled CF with Z_{st} = 0.183, a = 52.6 /s, and T_{max}≈2000 K [50–53] are also roughly threefold smaller than the measured values (see Table 1) [50]. The approximately 200 K higher T_{max} of the literature CFs compared to the considered PMLF compensates for its larger a and results in approximately equal measured and computed $X_{A1,max}$ in the two flames which have similar incipiently sooting loads.

It appears that experiments in PMLFs enable testing chemical kinetic models in a broader range of a and T_{max} compared to that in CFs and all flaws of chemical kinetic models are likely to be amplified for PAHs in the challenging long residence time conditions established in the PMLF, especially when one considers species further down the chain of reactions initiated by ethylene oxidation and pyrolysis. Fig. 8 shows the profiles of C8-C18 aromatics in the PMLF at HAB= 25 mm and 50 mm and compares the measurements to the predictions of ABF which is the only of the two tested chemical kinetic models accounting for the formation of some (but not all) of the quantitated heavy PAHs. One can notice that ABF in 2D-CFD predicts noticeably larger X_is but similar profile shapes for most aromatics compared to the equivalent 1D-CF, the difference being within a 2-factor in all cases but at $x < 0$ for aromatics with oxygen functional groups such as phenol. The underprediction of 1D-CF compared to 2D-CFD is not surprising since benzene which is the main starting point for aromatic growth, is also underpredicted (see Table 1 and Fig.S7). The overlapping of the profile shapes predicted by 1D-CF and 2D-CFD which is apparent for most aromatics in Fig. 8 excluding phenol, indicates that the 2D advective leakage does not affect aromatics (neither directly nor indirectly) other than the oxygenated ones that may be formed via reactions with the H_2O_2 and HO_2 leaking from the PMLF leading edge (see Fig. 6). Instead, the slight polydispersity of the T advection histories of the PMLF reactant streams discussed in Section 3.4, may contribute significantly to the X_is of aromatics in 2D-CFD being larger (but with the same profile shapes) compared to that in the equivalent 1D-CF which, instead, has monodisperse histories in both streams of reactants. ABF [19,80] emphasizes the aromatic growth via the HACA mechanism [18] and, in 2D-CFD, closely reproduces the experimental results for most aromatics (i.e., phenol, phenylacetylene, styrene, naphthalene isomers, acenaphthylene, and phenanthrene) even if it underpredicts benzene by approximately 30 % at HAB= 50 mm (see Table 1) and overestimates (approximately twofold) acenaphthylene at both HABs, compared to measurements. Even the predictions of pyrene, the heaviest PAH considered by ABF, are within a 1.5 factor from the experimental results. The most significant flaw of ABF is the large (hundred times) underestimation of fluoranthene which is the heaviest PAH with a 5-membered ring it considers. Recent work suggests that 5-membered ring PAHs may be mechanistically important in soot formation [35] and the experimental results in Fig. 8 include the quantitation of quite heavy species of this type being present in the PMLF. For example, approximately 100 ppb of methyl-fluoranthene and cyclopenta[cd]pyrene isomers are measured at both HAB= 25 mm and 50 mm.

The comparison of the results at HAB= 25 mm and 50 mm in Figs. 7-8 enables the visualization of the slight broadening of the self-similar profiles caused by the boundary layer growth (Fig. 4) and the underlying decrease in the flame strain rate at increasing HABs. ABF in 2D-CFD predicts a slight reduction of the X_i of most aromatic species at HAB= 50 mm compared to 25 mm. The reduction at increasing HABs is not predicted by the equivalent 1D-CF for most aromatics and, therefore, is likely caused by the 2D effects. 2D-CFD likely overestimates such 2D effects since the reduction is not noticeable in the experimental results. Instead, most of the experimental profiles in Fig. 8 exhibit the same if not higher peak values at HAB= 50 mm compared to 25 mm. This indicates that the chemistry of most aromatics is insensitive to the slight change in the strain rate from 7.0 /s to 9.8 /s, a behavior that is predicted by ABF in 1D-CF, or that the 2D effects are compensated by reactions not considered by ABF, enhanced at increasing residence times. Indeed, naphthalene isomers, acenaphthylene, anthracene, cyclopenta[def] phenanthrene, and the isomers of methyl-pyrene are slightly more

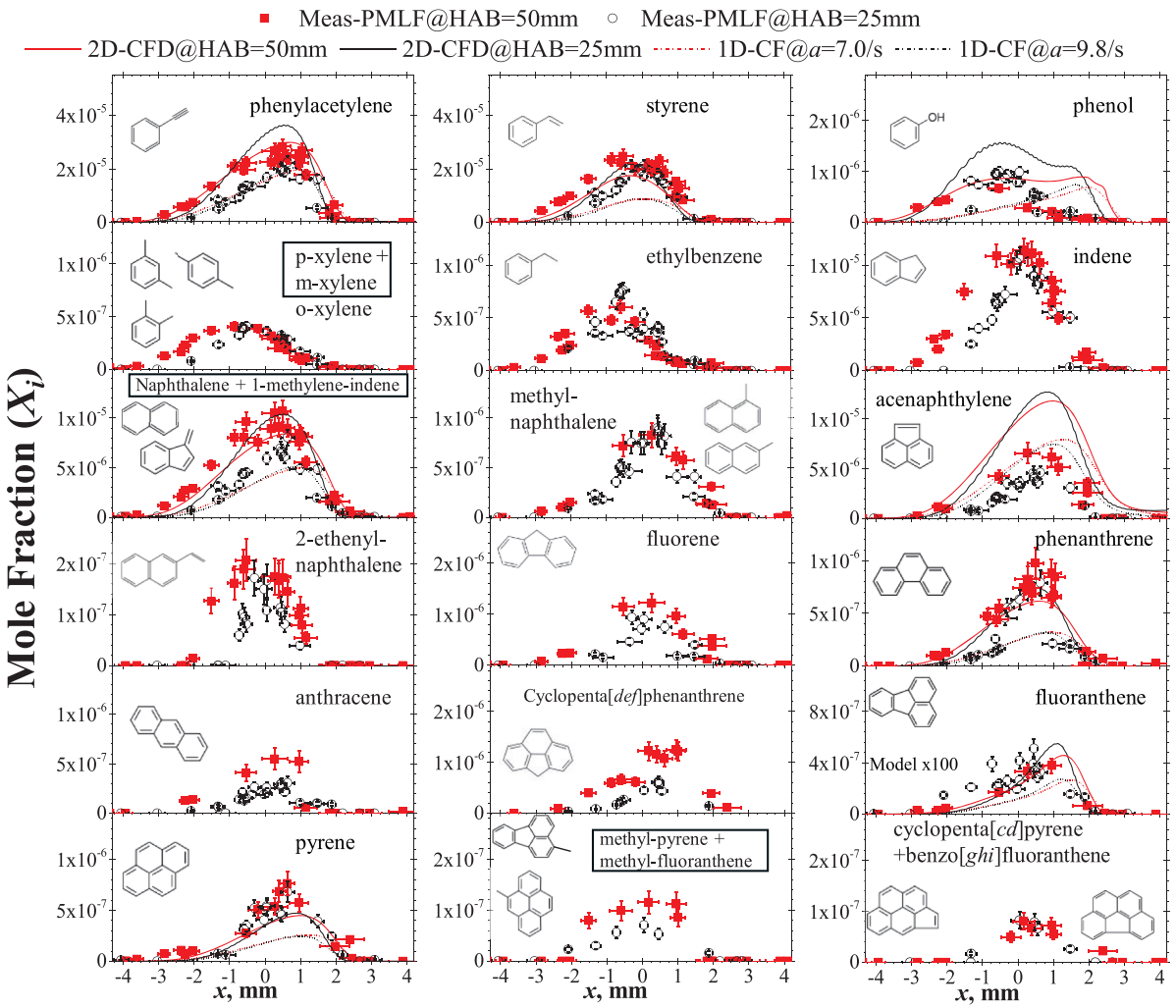

Fig. 8. Measured and computed profiles of C8-C18 aromatics at HAB= 25 mm and 50 mm. Computations are performed by 2D-CFD and equivalent 1D-CFs with the modified ABF [19,80]. All isomers (but those grouped with a square in the legend) are measured individually (see Fig. S8 in SM) but have been lumped during the processing of the results to ease the comparisons with the models. The abscissa is the distance (x) from the GMI in the PMLF cross-sections or the GSP in the equivalent 1D-CFs.

abundant at HAB= 50 mm compared to 25 mm. This observation is not affected by uncertainty since the increase is observed across the entire width of the profiles and for two species, one (acenaphthylene) being formed from the other (naphthalene isomers) via acetylene addition (i.e., HACA). Therefore, the difference is likely caused by a reaction path producing naphthalene which is enhanced at low strain rates and long residence times but is not considered by ABF, such as cyclopentadienyl recombination [20,21]. Additionally, an enhanced addition of cyclopentadienyl to indene, naphthalene isomers, and acenaphthylene may also cause the observed $X_{i,max}$ increase of anthracene, cyclopenta[def] phenanthrene, and the isomers of methyl-pyrene, respectively.

Benzene is the most abundant aromatic at both HAB= 25 mm and 50 mm with $X_{A1,max} \approx 150$ ppm which is more than one and two orders of magnitude more abundant than naphthalene and heavier PAHs such as pyrene, respectively. Some recent studies indicate that small aromatics (i.e., as heavy as acenaphthylene) may participate directly in soot inception in ethylene-fueled CFs [32,56] and burner-stabilized premixed flames [36]. This is in contrast to the widespread assumption that only PAHs as heavy and heavier than pyrene may cause soot inception. The experimental data included in Fig. 8 suggest that small hydrocarbons may be relevant to soot inception also in the investigated ethylene-fueled PMLF. Indeed, the concentrations of aromatics heavier than pyrene are far too little for them to contribute directly to a significant fraction of the incipient soot nanoparticles which are expected in numbers of the order of $10^{12} - 10^{13}$ cm^{-3} [32,36,89].

In summary, the data shown in Figs. 5-7 and 8 (and S4-S7) and Table 1 demonstrates the excellent capability of the equivalent 1D-CF to mimic the structure of the horizontal cross-sections of the PMLF at HAB= 25 mm and 50 mm at a small fraction of the computational cost of 2D-CFD and with reasonable quantitative accuracy even for heavy PAHs. The relatively small imprecision of the equivalent 1D-CF is a more than worthy price to pay, especially if one considers that the savings in terms of computational cost enable one to perform path and sensitivity analyses of complex kinetic models [90,91] that would be otherwise prohibitive in 2D-CFD.

3.4. *Thermochemical advection histories in the PMLF and equivalent 1D-CFs*

An additional analysis of the PMLF flow structure based on 2D-CFD results is necessary to assess if the equivalence between the PMLF horizontal cross-sections and 1D-CF is limited to diffusion transport, as shown in Sections 3.1-3.3, or applies at least approximately, also to the thermochemical advection histories experienced by the flame products. To this end, Fig. 9 shows finely spaced gas advection streamlines (gray dotted-dashed lines) computed by 2D-CFD with ABF. The streamlines

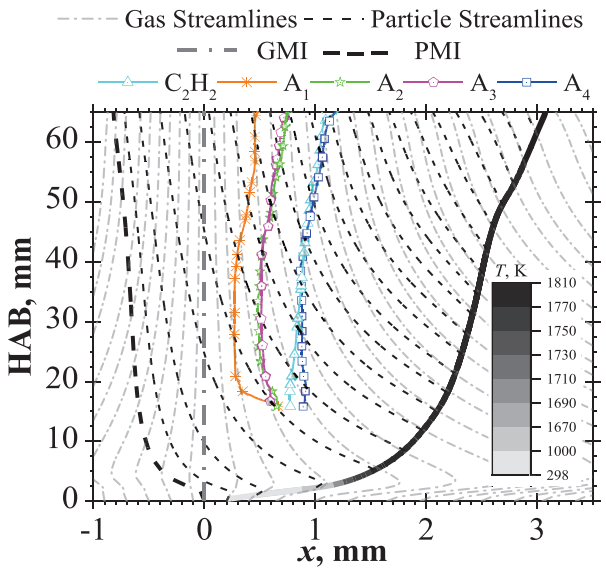

Fig. 9. Flow structure of the PMLF predicted by 2D-CFD with modified ABF [19,80], as depicted by gas streamlines (dotted-dashed lines) and the sections of the particle streamlines (dotted lines) lying in the soot-laden region between T_{max} (grayscale-coded thick solid line) and the Particle Mixing Interface (PMI). The abscissa is the horizontal distance from the GMI ($x@HAB = \bar{x} - \bar{x}_{GMI}@HAB$). The PMI is the particle streamline originating from the splitter between the fuel and oxidizer nozzles. The streamlines are superimposed to solid lines tracking the position of T_{max} (grayscale-coded value) and $X_{i,max}$ of acetylene (C_2H_2), benzene (A1), naphthalene (A2), phenanthrene (A3), and pyrene (A4) in the PMLF horizontal cross-sections.

are plotted as a function of the horizontal distance from the GMI at increasing HABs (i.e., $x@\text{HAB} = \bar{x} - \bar{x}_{GMI}@\text{HAB}$), instead of the absolute horizontal coordinate $\bar{x}$ which is used for the coarsely spaced gas streamlines of Fig. 3. As a result of the x-axis choice, the GMI is the thickest vertical gas streamline at $x = 0$ in Fig. 9, allowing one to visualize the positioning of the self-similar profiles shown in Figs. 5-8. The choice of the x-axis also nullifies the distorting displacement of the GMI toward the fuel stream (i.e., to the left) at increasing HABs below 5 mm apparent in Fig. 3, which is caused by the thermal expansion ensuing heat release in the oxidizer stream to the right of the GMI. In Fig. 11, the heat release rate-induced thermal expansion causes only the initial divergence of the gas streamlines at increasing HABs below 5 mm before they start converging toward the GMI under the effect of buoyant acceleration. The gas streamlines are superimposed to solid lines tracking the position of T_{max} (thick line with grayscale-coded value) and $X_{i,max}$ of five species involved in fuel pyrolysis and ensuing soot inception, namely acetylene (C_2H_2), benzene (A1), naphthalene (A2), phenanthrene (A3), and pyrene (A4). The lines tracking $X_{i,max}$ are not shown at HAB <16 mm where the 2D-CFD with ABF predicts their $X_{i,max}$ to be negligibly small and soot is not visible in digital images (Figs. 3-4).

Additionally, Fig. 9 depicts the particle streamlines (dashed lines) computed by considering the particle velocity ($\overrightarrow{V_p}$) field. The latter differs from the gas velocity ($\overrightarrow{V_g}$) field because of the thermophoretic drift velocity ($\overrightarrow{V_{th}}$) whose field for particles small enough to be in the free molecular regime, such as incipient soot, is determined by the fields of the temperature gradient ($\vec{\nabla}T$) and kinematic viscosity (ν) of the gas mixture [92,93]:

$$\overrightarrow{V_p} = \overrightarrow{V_g} + \overrightarrow{V_{th}} = \overrightarrow{V_g} - 0.538 \cdot \nu \cdot \frac{\vec{\nabla}T}{T} \quad (1)$$

The particle streamlines are plotted exclusively in the soot-laden region of the PMLF which, according to the structure depicted in Figs. 3-8, is the carbon-rich one to the left (i.e., downstream) of T_{max}. The particle streamline which originates from $\bar{x}$=0 at HAB = 0 is sandwiched between those yielding from the oxidizer and fuel nozzles and is named the Particle Mixing Interface (PMI). The PMI is expected to delimit the soot-laden region because to its left T drops below 1030 K which is considered too low for activating soot inception in the fuel stream [10,12,24,25,27–32]. It is noteworthy to mention that the horizontal span of the zone between T_{max} and PMI identified in Fig. 9 is nearly equal to the measured thickness of the PMLF luminous soot layer δ_{soot} in Fig. 4. Only a very small fraction of the smallest soot nanoparticles may cross the PMI via Brownian diffusion although the value of their diffusivity is substantially smaller compared to that of PAHs. In brief, the PMI of the PMLF is equivalent to the Particle Stagnation Plane (PSP) of 1D-CFs [52–56] and the horizontal distance of the PMI from the GMI in the PMLF is also equal to that of the PSP from the GSP in the equivalent 1D-CF. It appears that the equivalence between the PMLF horizontal cross-sections and 1D-CFs apply also to the advection of incipient soot particles.

A careful observation of Fig. 9 reveals that the $X_{i,max}$s of the selected species are all located within the soot-laden region with those of acetylene and benzene being the closest to T_{max} (i.e., the most upstream) and the GMI (i.e., the furthest downstream), respectively. The $X_{i,max}$s of aromatics of increasing molecular weight are sorted from left to right (i.e., from downstream to upstream) as predicted by the results of both 2D-CFD and equivalent 1D-CF results which are validated by experiments in Figs. 5-8 and Table 1. Therefore, in both PMLF and equivalent 1D-CFs, aromatic growth and ensuing soot inception take place in a non-sequential manner during the advection of the flame products. Instead one should consider both advection and diffusion transport to rationalize the relative position of the $X_{i,max}$ in Fig. 9. To begin with, acetylene is mostly produced by the dehydrogenation of the ethylene fuel that is promoted at high Ts. Nonetheless, ethylene crosses the GMI via diffusion from the fuel stream and is increasingly less abundant away from it. As a result, acetylene production is maximum somewhere in between T_{max} and GMI whereas the production of A1 occurs downstream (i.e., to the left) compared to that of acetylene and other (mostly C2-C4) fuel pyrolysis products, indicating that A1 production has a significant induction time. Next, all subsequent aromatic growth reactions are enhanced at increasing Ts, are fast compared to A1 production, and require acetylene (as well as other C1-C5 fuel pyrolysis products). As a result, the optimal conditions for A2 production are established via the back diffusion of A1 from its $X_{A1,max}$ peak toward $X_{C2H2,max}$ and T_{max}. By reiteration of the back diffusion of aromatics to which acetylene (and other fuel pyrolysis products) are added the production of progressively heavier PAHs is maximized closer and closer to $X_{C2H2,max}$ and T_{max}. Consequently, the $X_{i,max}$ of A4 which is the heaviest PAH considered by ABF, occurs roughly at the same position as $X_{C2H2,max}$.

At this stage, one could wonder about the actual thermochemical histories the gas parcels experience in the PMLF while they are advected along each gas streamline depicted in Fig. 9. Additionally, given the similarity between the PMLF horizontal cross-sections and their equivalent 1D-CFs, one would like to compare them with the monodisperse advection histories the gas parcels yielding from either the fuel or oxidizer nozzle experiences in the equivalent 1D-CFs [51–52,55]. The dotted lines in Fig. 10 present the profiles of T and X_is of CO_2, H_2O, CO, H_2, acetylene, and selected PAHs the gas parcels experience to reach HAB= 50 mm as a function of the advection time (t_{gas}) calculated as the integral of the inverse of the velocity magnitude along different gas streamlines equispaced at the PMLF fuel (left panels) and oxidizer (right panels) nozzles. The t_{gas} zero is set along each gas streamline at the point where 2D-CFD predicts the local X_{C2H2} to be 75 % of its value on the GMI (i.e., at $x = 0$) at HAB= 50 mm. Such a point is crossed by each gas streamline a bit upstream of the PMI which is positioned at $t_{gas} \approx 7 \pm 3$ ms in the left panel of Fig. 10, and slightly downstream of T_{max} which is not shown but would be found at $t_{gas} \approx -10 \pm 5$ ms in the right panel of Fig. 10, in the fuel and oxidizer streams, respectively. In brief, Fig. 10 depicts the thermochemical advection histories the gas parcels

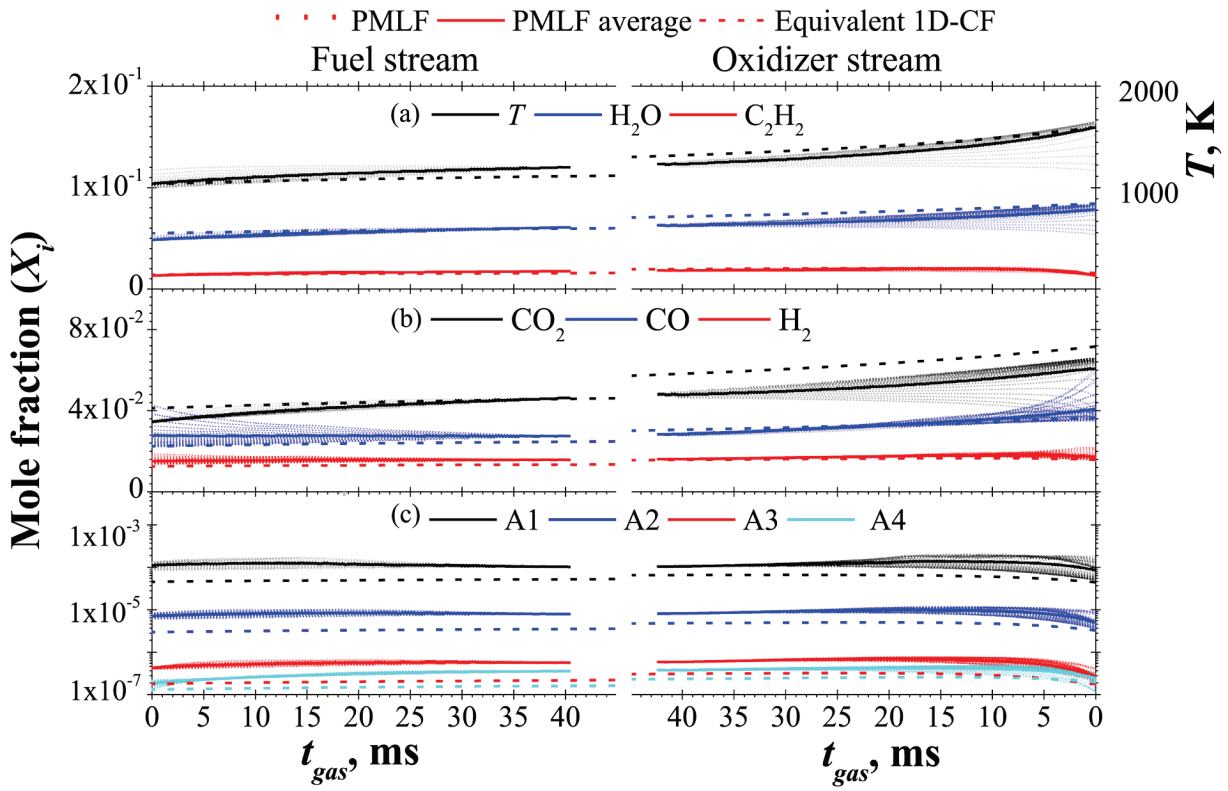

Fig. 10. Thermochemical histories the gas parcels experience as a function of the advection time (t_{gas}) either in the PMLF (dotted lines) while they reach HAB=50 mm or in the equivalent 1D-CF (dashed lines). Solid lines show the averages of the slightly polydisperse PMLF thermochemical histories to ease the comparison with 1D-CF. The t_{gas} zero is at the position along each streamline where 2D-CFD predicts the local X_{C2H2} to be 75 % of its value on the GMI (i.e., at $x = 0$) at HAB= 50 mm.

experience within the entire PMLF before contributing to the structure of the soot-laden zone in the PMLF cross-section at HAB= 50 mm. For the sake of completeness, the thermochemical advection histories leading to the structure of the PMLF at HAB =25 mm and its equivalent 1D-CF are shown and compared in Fig. S9 of SM.

For comparison, the dashed lines in Fig. 10 show the monodisperse thermochemical advection histories experienced by any gas parcel yielding from the fuel and oxidizer streams in the 1D-CF equivalent to the PMLF at HAB= 50 mm. To ease the visual comparison between the PMLF and 1D-CF, the solid lines depict the average T and X_is for all gas streamlines in the PMLF at any t_{gas}. Such averages do not differ significantly from the mass-averaged thermochemical properties of the whole fuel and oxidizer streamtubes. Indeed, the streamlines are equispaced at the outlet of the fuel and oxidizer nozzles where the mass flux and composition are uniform. The comparison confirms a close agreement between the thermochemical advection histories established in PMLF and equivalent 1D-CF. The average T-t_{gas} (panel a) in the PMLF differs at most 87 K from that in 1D-CF, the latter being slightly colder and hotter than the former in the fuel and oxidizer streams, respectively. The differences are similarly minor for X_{C2H2} and X_{H2O} (panel a) and X_{CO} and X_{H2} (panel b) whose averages in the PMLF differ less than 11 % compared to that in the 1D-CF. The most evident deviation for C0-C2 species is noticeable for X_{CO2} (panel b) but only in the oxidizer stream where it is approximately 16 % lower in the PMLF compared to 1D-CF. The difference is likely related to the average T-t_{gas} of the oxidizer stream (where oxidation reactions take place) being slightly colder in the PMLF than in the equivalent 1D-CF. Still, such a difference in X_{CO2} is not expected to affect significantly the kinetics of soot inception. Turning attention to the advection histories in the bottom panel (c), it is known that the X_is of PAHs are very sensitive to even small changes in the T-t_{gas} [49]. It appears that the slight polydispersity of the T-t_{gas} histories experienced along different streamlines of the PMLF causes an enhancement in the formation of most aromatics (see Fig. 8) since the 1D-CF predicts their X_is to be approximately twofold smaller compared to 2D-CFD. Nonetheless, the imprecision of the equivalent 1D-CF model compared to 2D-CFD is a more than worthy price to pay if one considers the savings in terms of computational cost. Indeed, 1D-CF not only mimics with reasonable accuracy the PMLF advection and diffusion transport but also enables the path and sensitivity analyses of complex kinetic models [90,91] that are prohibitive to implement in 2D-CFD.

3.5. Reaction pathway analyses in PMLF equivalent 1D-CFs

Reaction path and sensitivity analyses of chemical kinetic models in canonical 1D flame configurations have become essential tools to improve their predictive capabilities [90,91]. Additionally, reaction path analyses can be used to pinpoint the effect of perturbing some boundary conditions of 1D-CFs on reactions relevant to PAHs and soot formation [48,50–52]. Initially, one may think that the 2D nature of PMLFs makes them unsuitable for performing such analyses which are difficult to implement and computationally prohibitive in 2D-CFD. Nonetheless, the previous sections demonstrated that the horizontal cross-sections of a PMLF can be modeled with reasonable accuracy as equivalent 1D-CFs with the same Z_{st} and T_{max} and the value of a that makes its thermal thickness equal to that of the PMLF at the selected HAB. The equivalent 1D-CF mimics the PMLF from both the diffusion and advection transport point of view and is readily amenable for reaction path and sensitivity analyses. The path analyses are performed by integrating the Rate Of Production (ROP) of the i-species of interest over the entire x span for each reaction considered in the chemical kinetic model. Net production (consumption) reactions have positive (negative) integral ROP. The percentage contribution of each production reaction is calculated by dividing its integral ROP by the sum of the integral ROP of all production reactions.

This section examines the effect of changing a from 7.0 /s to 50 /s while keeping constant Z_{st} = 0.183 and T_{max}=1786 K, on the reaction

pathways leading to the formation of benzene (A1) from the parent ethylene fuel. The largest considered value of $a = 50$ /s is typical of 1D-CF experiments whereas $a = 7.0$ /s makes the 1D-CF equivalent to the cross-section at HAB= 50 mm of the PMLF characterized herein. The analyses are performed using USC which has good performances in predicting the concentration of C0-C4 flame intermediates playing a critical role in the formation of benzene and, subsequently, heavier aromatics. Also, USC yields almost identical results in either 2D-CFD or equivalent 1D-CF, as depicted in Table 1 and Figs. 5-8. The reaction path analyses of 1D-CF with $a = 9.8$ /s equivalent to the PMLF cross-section at HAB= 25 mm are relegated to SM (Fig.S10) because they yield very similar results as for $a = 7.0$ /s. The SM presents also the path analyses performed with ABF which is somewhat less reliable in predicting C0-C4 species (see Table 1 and Figs.S3-S7), upon considering the reactions leading to the production of benzene (Fig. S11) as well as those causing its subsequent growth to form PAHs (Fig.S12).

The results of path analyses are summarized in Fig. 11 in which each solid arrow is coupled to a number that quantifies the total contribution percentage of reactions involving the reactant at the arrow origin, to the production of the product the arrow points to. The percentage refers to 1D-CF with $a = 7.0$ /s equivalent to the PMLF at HAB= 50 mm and is followed by a second percentage in parentheses which refers to a 1D-CF with $a = 50$ /s typical of CF experiments. Some dashed arrows run parallel to the solid ones to identify a significant reaction partner contributing to the considered reactant-to-product conversion. The red bold font identifies the stable species quantified in the experiments and for which USC showed relatively good predictive performances (see Figs. 5 and 7 and Table 1). One can assume that the USC predictions of carbonaceous radical species are as accurate as those of their stable counterparts. For example, the accuracy in predicting the methyl, vinyl, ethyl, and propargyl (C_3H_3) radicals is expected to be similar to that of the predictions of methane, ethylene, ethane, and C_3H_4 isomers, respectively. Cancellations of errors are always possible but are unlikely to be significant for such small radicals that are prevalently formed via hydrogen abstraction reactions, as evidenced in Fig. 11.

Fig. 11 highlights that A1 is produced mainly via two pathways namely C_3H_3 recombination and reactions of C4 with C2 species (i.e., $C_4H_5 + C_2H_2$ and $C_4H_6 + C_2H_3$). The relevance of these two paths in flames fueled by linear aliphatics is well documented in the literature [18–21,24,25,29–31,35,94,95] but different kinetic models may emphasize one over the other. For example, ABF underplays the contribution of C_3H_3 recombination because of the high energy required for cyclization and hydrogen redistribution to form A1 from the C_3H_3–-C_3H_3 adduct [95]. However, many studies have shown that C_3H_3 recombination can contribute substantially to A1 in most flame conditions thanks to the resonant stabilization which makes C_3H_3 persistent with relatively large X_{C3H3}s (e.g., Fig. 6) [94]. Fig. 11 shows that, according to USC and regardless of the value of a, C_3H_3 formation is caused overwhelmingly, and in approximately constant proportions, by H abstraction from C_3H_4 isomers and by either direct or indirect methylidyne addition to acetylene. USC predicts acetylene accurately whereas it underpredicts the total X_is of C_3H_4 isomers (mostly allene) by approximately twofold (Fig. 7). Also, C_4H_5 is mainly produced via H-abstraction from the isomers of 1,3-butadiene (C_4H_6) whose (lumped) X_{C4H6} profile is also well predicted by USC (Fig. 7).

Most importantly, Fig. 11 highlights that the lowering of a from 50 /s to 7.0 /s, whose experimental investigation is enabled in the PMLF, leads to an approximately 50 % enhancement of the relative contribution of C_3H_3 recombination to form A1 either directly or through the addition of the H radical to the so formed phenyl radical. Concurrently and consequently, the relative contribution of the C4+C2 reactions is predicted to be halved. If one considers that USC underpredicts C_3H_4 roughly twofold (therefore, it is likely to underpredict also C_3H_3) but is accurate in predicting C_4H_6 which is the most relevant starting point of the C4+C2

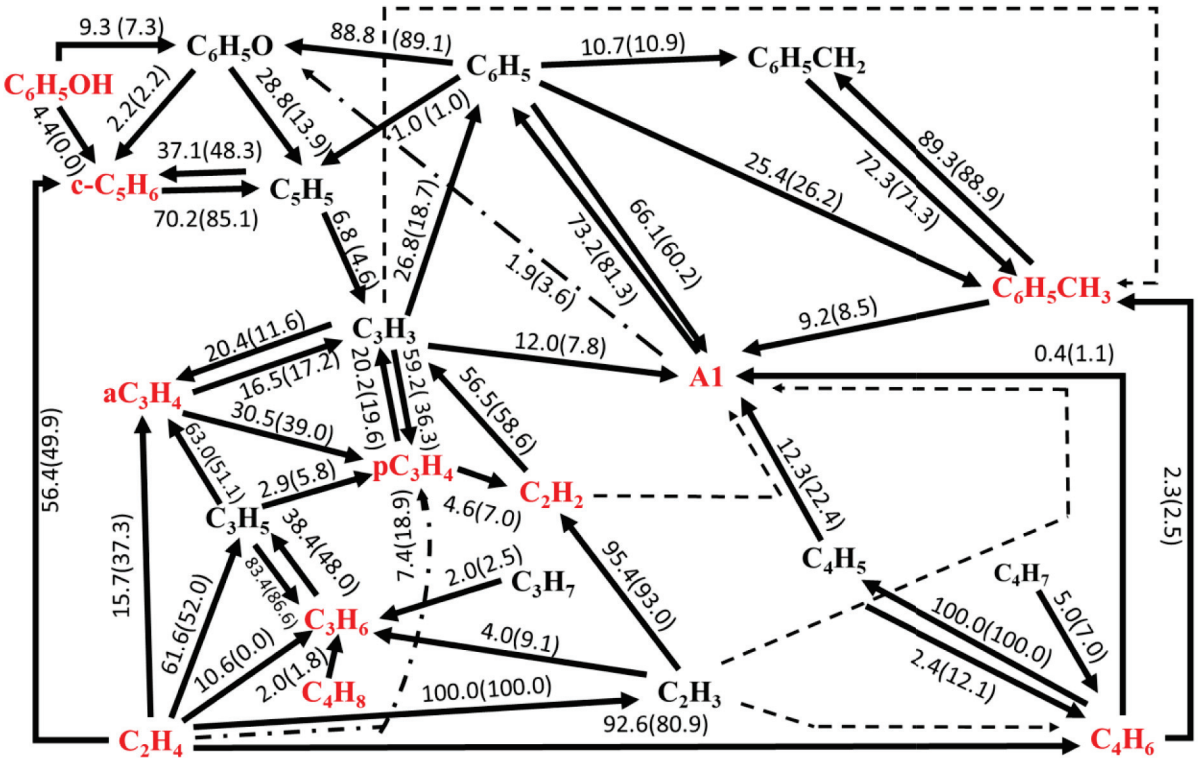

Fig. 11. Pathway analyses of the USC [79] reactions forming benzene (A1) in 1D-CF with Z_{st}=0.183, T_{max}=1776 K, and $a = 7.0$ /s equivalent to the PMLF at HAB= 50 mm (or $a = 50$ /s typical of CF experiments). Each solid arrow connects a reactant to a product and is coupled to a number listing the percentage the identified reactions contribute to the product for $a = 7.0$ /s ($a = 50$ /s). Dashed arrows identify significant reaction partners and the red bold font highlights the species that have been quantified in the experiments.

pathways, it is plausible that the relative enhancement of the C_3H_3 pathway is partially responsible for the roughly threefold underprediction of benzene. It is also possible that additional pathways leading to benzene formation are not considered by USC but they may become increasingly more relevant when lowering a from 50 /s to 7.0 /s and, therefore, in PMLF compared to CF experiments.

In summary, the PMLF experimental results reported in this manuscript are instrumental in quantifying the enhancement of any reaction as well as in identifying any potentially unaccounted pathways that are active in non-premixed flame characterized by low strain rates and advection time of the order of tens of milliseconds. Therefore, the study of PMLFs may contribute substantially to the improvement of the predictive capabilities of any chemical kinetic models in a range of sooting and non-sooting flame conditions that are relevant to several non-premixed combustion applications but not accessible in experiments performed in other canonical flame configurations.

4. Conclusions

An incipiently sooting laminar Planar Mixing Layer Flame (PMLF) accessible to intrusive sampling has been stabilized by introducing a buoyancy-driven passive flow stabilization. The PMLF structure has been investigated experimentally using capillary sampling followed by GC/MS analyses, fine thermocouple measurements, and digital imaging. Computationally, two detailed chemical kinetic models are used in a 2D-CFD model of the PMLF and a 1D model of Counterflow Flames (CFs) equivalent to selected PMLF horizontal cross-sections. The PMLF equivalent 1D-CF has the same stoichiometric mixture fraction (Z_{st}), maximum temperature (T_{max}), and thermal thickness as the PMLF at the selected Height Above the Burner (HAB).

The main findings follow below.

- The PMLF thickens at increasing HABs and remains very stable while being probed by capillary sampling, horizontal tube dilution sampling, or a fine thermocouple.
- There is a self-similarity between the horizontal cross-sections of the PMLF and 1D-CFs with the same Z_{st} but the PMLF is three times thicker than CFs suitable for experimental studies.
- Thanks to its boundary layer structure and large thicknesses, the PMLF is amenable to being sampled with any type of intrusive probe without sacrificing the spatial resolution necessary to follow the kinetics of fuel oxidative pyrolysis and soot inception.
- The structures of the PMLF horizontal cross-sections at HAB= 25 mm and 50 mm have been characterized experimentally by quantifying temperature and the mole fractions of forty-five species. The dataset can be used as a testbed to improve chemical kinetic models.
- The horizontal cross-sections of the PMLF can be modeled as an equivalent 1D-CF with strain rates not achievable in 1D-CF experiments. The equivalence greatly simplifies the testing of chemical kinetic models but causes slight (mostly less than twofold) underpredictions of species with highly temperature-sensitive kinetics such as aromatics.
- The 2D effects include a minor leakage in the fuel stream of some species from the PMLF leading edge which affects moderately only oxygenated species, and a slight polydispersity of the advection histories which impacts (mostly less than twofold) the predictions of aromatics.
- Reaction pathway analyses in the equivalent 1D-CF assess the impact of lowering the strain rate from values typical of CF experiments to that of the PMLF on the reactions leading to benzene formation. Results show an enhancement of propargyl recombination and suggest that some reactions active at low strain rates may be not considered in the tested kinetic models.
- The PMLF is a promising canonical configuration to perform detailed experimental studies of combustion chemistry and soot inception in non-premixed flames with low strain rates and on time scales of tens of milliseconds which are relevant to many combustion applications.

CRediT authorship contribution statement

Mahmoud K. Ashour: Writing – review & editing, Writing – original draft, Visualization, Validation, Software, Investigation, Data curation. **Francesco Carbone:** Writing – review & editing, Writing – original draft, Visualization, Validation, Supervision, Software, Resources, Project administration, Methodology, Investigation, Funding acquisition, Formal analysis, Data curation, Conceptualization.

Declaration of competing interest

The authors declare that they have no known competing financial interests or personal relationships that could have appeared to influence the work reported in this paper.

Acknowledgments

This work is funded by the USA National Science Foundation (Grant #CBET-2013382, Program Manager Prof. Harsha K. Chelliah). The authors are thankful to Mr. Thomas Mealy for machining some components of the experimental system at the University of Connecticut (UConn) and acknowledge preliminary 2D-CFD computations and burner prototyping performed at UConn as an honor thesis by Carmen Ciardiello and a senior design project by Celia Chako, respectively.

Supplementary materials

Supplementary material associated with this article can be found, in the online version, at doi:10.1016/j.combustflame.2024.113537.

References

[1] International Energy Agency (IEA), World energy outlook 2022. https://www.iea.org/reports/world-energy-outlook-2022 (2022). (accesed 11/18/2023).
[2] USA Energy Information Administration (EIA), Annual energy outlook 2023. https://www.eia.gov/outlooks/aeo/(2023), (accessed 11/18/2023).
[3] USA Energy Information Administration (EIA), International energy outlook 2023. https://www.eia.gov/outlooks/ieo/(2023), (accessed 11/18/2023).
[4] J.S. Lighty, J.M. Veranth, A.F. Sarofim, Combustion aerosols: factors governing their size and composition and implications to human health, J. Air Waste Manag. Assoc. 50 (2000) 1565–1618.
[5] N.A.H. Janssen, M.E. Gerlofs-Nijland, T. Lanki, R.O. Salonen, F.R. Cassee, G. Hoek, P. Fischer, B.B. van Bree, M. Krzyzanowski, WHO Report, World Health Organization, Copenhagen, Denmark, 2012.
[6] B. Frank, R. Schlögl, D.S. Su, Diesel Soot toxification, Environ. Sci. Technol. 47 (2013) 3026–3027.
[7] A. Nel, T. Xia, L. Mädler, N. Li, Toxic potential of materials at the nanolevel, Science 311 (2006) 622–627.
[8] P. Pedata, T. Stoeger, R. Zimmermann, A. Peters, G. Oberdörster, A. D'Anna, Are we forgetting the smallest, sub 10 nm combustion generated particles? Part. Fibre. Toxicol. 12 (2015) 1–4.
[9] D. Shindell, G. Faluvegi, Climate response to regional radiative forcing during the twentieth century, Nat. Geosci. 2 (2009) 294–300.
[10] I. Glassman, Combustion, Academic Press, New York, USA, 1977.
[11] I.M. Miller, H.G. Maahs, High Pressure Flame System For Pollution Studies With Results For Methane-Air Diffusion Flames, NASA Langley research center, Hampton VA, USA, 1977. Report No. D-P8407.
[12] B.S. Haynes, H.G. Wagner, Soot formation, Prog. Energy Combust. Sci. 7 (1981) 229–273.
[13] J.H. Kent, H. Jander, H.G. Wagner, Soot formation in a laminar diffusion flame, Symp. (Int.) Combust. 18 (1981) 1117–1126.
[14] U. Vandsburger, I.M. Kennedy, I. Glassman, Sooting counter-flow diffusion flames with varying velocity gradients, Symp. (Int.) Combust. 20 (1985) 1105–1112.
[15] K.C. Smyth, J.H. Miller, R.C. Dorfman, W.G. Mallard, R.J. Santoro, Soot inception in a methane/air diffusion flame as characterized by detailed species profiles, Combust. Flame 62 (1985) 157–181.
[16] J. Du, R.L. Axelbaum, The effect of flame structure on soot-particle inception in diffusion flames, Combust. Flame 100 (1995) 367–375.
[17] I.M. Kennedy, C. Yam, D.C. Rapp, R.J. Santoro, Modeling and measurements of soot and species in a laminar diffusion flame, Combust. Flame 107 (1996) 368–382.

[18] H. Wang, M. Frenklach, A detailed kinetic modeling study of aromatics formation in laminar premixed acetylene and ethylene flames, Combust. Flame 110 (1997) 173–221.
[19] J. Appel, H. Bockhorn, M. Frenklach, Kinetic modeling of soot formation with detailed chemistry and physics: laminar premixed flames of C2 hydrocarbons, Combust. Flame 121 (2000) 122–136.
[20] H. Richter, J.B. Howard, Formation of polycyclic aromatic hydrocarbons and their growth to soot—A review of chemical reaction pathways, Prog. Energy Combust. Sci. 26 (2000) 565–608.
[21] A. Violi, A. D'Anna, A. D'Alessio, A.F. Sarofim, Modeling aerosol formation in opposed-flow diffusion flames, Chemosphere 51 (2003) 1047–1054.
[22] C.S. McEnally, L.D. Pfefferle, B. Atakan, K. Kohse-Höinghaus, Studies of aromatic hydrocarbon formation mechanisms in flames: progress towards closing the fuel gap, Prog. Energy Combust. Sci. 32 (2006) 247–294.
[23] M. Yamamoto, S. Duan, S. Senkan, The effect of strain rate on polycyclic aromatic hydrocarbon (PAH) formation in acetylene diffusion flames, Combust. Flame 151 (2007) 532–541.
[24] A. D'Anna, Combustion-formed nanoparticles, Proc. Combust. Inst 32 (2009) 593–613.
[25] H. Wang, Formation of nascent soot and other condensed-phase materials in flames, Proc. Combust. Inst 33 (2011) 41–67.
[26] A.E. Karataş, Ö.L. Gülder, Soot formation in high pressure laminar diffusion flames, Prog. Energy Combust. Sci. 38 (2012) 818–845.
[27] H.A. Michelsen, Probing soot formation, chemical and physical evolution, and oxidation: a review of in situ diagnostic techniques and needs, Proc. Combust. Inst. 36 (2017) 717–735.
[28] K. Johansson, M. Head-Gordon, P. Schrader, K. Wilson, H. Michelsen, Resonance-stabilized hydrocarbon-radical chain reactions may explain soot inception and growth, Science (1979) 361 (2018) 997–1000.
[29] Y. Wang, S.H. Chung, Soot formation in laminar counterflow flames, Prog. Energy Combust. Sci. 74 (2019) 152–238.
[30] H.A. Michelsen, M.B. Colket, P.E. Bengtsson, A. D'anna, P. Desgroux, B.S. Haynes, J.H. Miller, G.J. Nathan, H. Pitsch, H. Wang, A review of terminology used to describe soot formation and evolution under combustion and pyrolytic conditions, ACS Nano 14 (2020) 12470–12490.
[31] R.S. Jacobson, A.R. Korte, A. Vertes, J.H. Miller, The molecular composition of soot, Angew. Chem. 132 (2020) 4514–4520.
[32] K. Gleason, F. Carbone, A.J. Sumner, B.D. Drollette, D.L. Plata, A. Gomez, Small aromatic hydrocarbons control the onset of soot nucleation, Combust. Flame 223 (2021) 398–406.
[33] J.W. Martin, M. Salamanca, M. Kraft, Soot inception: carbonaceous nanoparticle formation in flames, Prog. Energy Combust. Sci. 88 (2022) 100956.
[34] M.J. Thomson, Modeling soot formation in flames and reactors: recent progress and current challenges, Proc. Combust. Inst. 39 (2022) 805–823.
[35] M. Frenklach, A.M. Mebel, Prenucleation chemistry of. aromatics: a two-ring precursor? Proc. Combust. Inst. 39 (2023) 825–833.
[36] F. Carbone, Kevin Gleason, A. Gomez, Soot research: relevance and priorities by mid-century, in: K. Brezinsky (Ed.), Combustion Chemistry and the Carbon Neutral Future, Elsevier, New York, 2023, pp. 27–61.
[37] T.S. Norton, K.C. Smyth, J.H. Miller, M.D. Smooke, Comparison of experimental and computed species concentration and temperature profiles in laminar, two-dimensional methane/air diffusion flames, Combust. Sci. Technol. 90 (1993) 1–34.
[38] J.D. Herdman, B.C. Connelly, M.D. Smooke, M.B. Long, J.H. Miller, A comparison of Raman signatures and laser-induced incandescence with direct numerical simulation of soot growth in non-premixed ethylene/air flames, Carbon 49 (2011) 5298–5311.
[39] E.M. Adkins, J.H. Miller, Extinction measurements for optical band gap determination of soot in a series of nitrogen-diluted ethylene/air non-premixed flames, Phys. Chem. Chem. Phys. 17 (2015) 2686–2695.
[40] A.A. Westenberg, S.D. Raezer, R.M. Fristrom, Interpretation of the sample taken by a probe in a laminar concentration gradient, Combust. Flame 1 (1957) 467–478.
[41] T. Pandya, F.J. Weinberg, The structure of flat, counter-flow diffusion flames, Proc. R. Soc. London, Ser. A 279 (1964) 544–561.
[42] A. Liñán, The asymptotic structure of counterflow diffusion flames for large activation energies, Acta Astronaut. 1 (1974) 1007–1039.
[43] S.K. Liew, K.N.C. Bray, J.B. Moss, A Flamelet Model of Turbulent Non-Premixed Combustion, Combust. Sci. Technol. 27 (1981) 69–73.
[44] S.K. Liew, K.N.C. Bray, J.B. Moss, A stretched laminar flamelet model of turbulent nonpremixed combustion, Combust. Flame 56 (1984) 199–213.
[45] N. Peters, Laminar diffusion flamelet models in non-premixed turbulent combustion, Prog. Energy Combust. Sci. 10 (1984) 319–339.
[46] N. Peters, Turbulent Combustion, Cambridge University Press, Cambridge, U.K., 2000.
[47] U. Niemann, K. Seshadri, F.A. Williams, Accuracies of laminar counterflow flame experiments, Combust. Flame 162 (2015) 1540–1549.
[48] F. Carbone, A. Gomez, Chemical interactions between 1,2,4-trimethylbenzene and n-decane in doped counterflow gaseous diffusion flames, Proc. Combust. Inst. 35 (2015) 761–769.
[49] L. Figura, F. Carbone, A. Gomez, Challenges and artifacts of probing high-pressure counterflow laminar diffusion flames, Proc. Combust. Inst. 35 (2015) 1871–1878.
[50] F. Carbone, F. Cattaneo, A. Gomez, Structure of incipiently sooting partially premixed ethylene counterflow flames, Combust. Flame 162 (2015) 4138–4148.
[51] F. Carbone, K. Gleason, A. Gomez, Pressure effects on incipiently sooting partially premixed counterflow flames of ethylene, Proc. Combust. Inst. 36 (2017) 1395–1402.
[52] K. Gleason, F. Carbone, A. Gomez, Effect of temperature on soot inception in highly controlled counterflow ethylene diffusion flames, Combust. Flame 192 (2018) 283–294.
[53] K. Gleason, F. Carbone, A. Gomez, Pressure and temperature dependence of soot in highly controlled counterflow ethylene diffusion flames, Proc. Combust. Inst. 37 (2019) 2057–2064.
[54] K. Gleason, F. Carbone, A. Gomez, Spatially resolved measurements of soot and gaseous precursors in ethylene counterflow diffusion flames up to 32 atm, Proc. Combust. Inst. 38 (2021) 2517–2524.
[55] Q. Wang, P. Elvati, D. Kim, K.O. Johansson, P.E. Schrader, H.A. Michelsen, A. Violi, Spatial dependence of the growth of polycyclic aromatic compounds in an ethylene counterflow flame, Carbon. N. Y. 149 (2019) 328–335.
[56] K. Gleason, F. Carbone, A. Gomez, PAHs controlling soot nucleation in 0.101—0.811MPa ethylene counterflow diffusion flames, Combust. Flame 227 (2021) 384–395.
[57] F.P. Incropera, D.P. DeWitt, T.L. Bergman, A.S. Lavine, Fundamentals of Heat and Mass Transfer, Wiley, New York, USA, 1996.
[58] B. Zhao, Z. Yang, M.V. Johnston, H. Wang, A.S. Wexler, M. Balthasar, M. Kraft, Measurement and numerical simulation of soot particle size distribution functions in a laminar premixed ethylene-oxygen-argon flame, Combust. Flame 133 (2003) 173–188.
[59] B. Zhao, Z. Yang, J. Wang, M.V. Johnston, H. Wang, Analysis of soot nanoparticles in a laminar premixed ethylene flame by scanning mobility particle sizer, Aerosol Sci. Technol. 37 (2003) 611–620.
[60] M. Maricq, Size and charge of soot particles in rich premixed ethylene flames, Combust. Flame 137 (2004) 340–350.
[61] R.A. Dobbins, C.M. Megaridis, Morphology of flame-generated soot as determined by thermophoretic sampling, Langmuir 3 (1987) 254–259.
[62] F.P. Hagen, P. Vlavakis, M. Seitz, T. Klövekorn, H. Bockhorn, R. Suntz, D. Trimis, Soot nanoparticle sizing in counterflow flames using in-situ particle sampling and differential mobility analysis verified with two-colour time-resolved laser-induced incandescence, Proc. Combust. Inst. 39 (2023) 1119–1128.
[63] A. Kalbhor, R. Schmitz, A. Ramirez, P. Vlavakis, F.P. Hagen, F. Ferraro, M. Braun-Unkhoff, T. Kathrotia, U. Riedel, D. Trimis, J. van Oijen, C. Hasse, D. Mira, Experimental and numerical investigation on soot formation and evolution of particle size distribution in laminar counterflow ethylene flames, Combust. Flame 260 (2024) 113220.
[64] A. Hamins, M. Bundy, C.B. Oh, S.C. Kim, Effect of buoyancy on the radiative extinction limit of low-strain-rate nonpremixed methane–air flames, Combust. Flame 151 (2007) 225–234.
[65] D. Zheng, A. Nobili, A. Cuoci, M. Pelucchi, X. Hui, T. Faravelli, Soot formation from n-heptane counterflow diffusion flames: two-dimensional and oxygen effects, Combust. Flame 258 (2023) 112441.
[66] H. Wolfhard, W. Parker, A new technique for the spectroscopic examination of flames at normal pressures, Proc. Phys. Soc. 62 (1949) 722–730.
[67] K.C. Smyth, P.H. Taylor, Detection of the methyl radical in a methane/air diffusion flame by multiphoton ionization spectroscopy, Chem. Phys. Lett. 122 (1985) 518–522.
[68] H. Miller, P.M. Taylor, Methyl radical concentrations and production rates in a faminar methane/air diffusion flame, Combust. Sci. Technol. 52 (1987) 139–149.
[69] K.C. Smyth, P.J.H. Tjossem, A. Hamins, J.H. Miller, Concentration measurements of OH· and equilibrium analysis in a laminar methane-air diffusion flame, Combust. Flame 79 (1990) 366–380.
[70] T.S. Norton, K.C. Smyth, Laser-induced fluorescence of CH · in a Laminar CH4/air diffusion flame: implications for diagnostic measurements and analysis of chemical rates, Combust. Sci. Technol. 76 (1991) 1–20.
[71] K.C. Smyth, P.J.H. Tjossem, Relative H-atom and O-atom concentration measurements in a laminar, methane/air diffusion flame, Symp. (Int.) Combust. 23 (1991) 1829–1837.
[72] K.C. Smyth, J.H. Miller, Chemistry of Molecular Growth Processes in Flames, Science (1979) 236 (1987) 1540–1546.
[73] F. Carbone, M. Attoui, A. Gomez, Challenges of measuring nascent soot in flames as evidenced by high-resolution differential mobility analysis, Aerosol Sci. Technol. 50 (2016) 740–757.
[74] M.V. Heitor, A.L.N. Moreira, Thermocouples and sample probes for combustion studies, Prog. Energy Combust. Sci. 19 (1993) 259–278.
[75] P. Jiang, M. Zhou, D. Wen, Y. Wang, An experimental multiparameter investigation on the thermochemical structures of benchmark ethylene and propane counterflow diffusion flames and implications to their numerical modeling, Combust. Flame 234 (2021) 111622.
[76] H.W. Coleman, W.G. Steele, Experimentation, validation, and Uncertainty Analysis For Engineers, John Wiley & Sons, New York, USA, 2018.
[77] S. Ahuja, D.L. Miller, Design of a constant tension thermocouple rake suitable for flame studies, Rev. Sci. Instrum. 64 (1993) 1358–1359.
[78] V.A. Cundy, J.S. Morse, D.W. Senser, Constant-tension thermocouple rake suitable for use in flame mode combustion studies, Rev. Sci. Instrum. 57 (1986) 1209–1210.
[79] H. Wang, X. You, A. Joshi, S. Davis, A. Laskin, F. Egolfopoulos, C. Law, USC Mech Version II, published in http://ignis.usc.edu/USC_Mech_II.htm, May 2007.
[80] M. Frenklach, Personal communication (2023).
[81] R.J. Kee, J. Warnatz, J.A. Miller, Fortran Computer-Code Package For the Evaluation of Gas-Phase viscosities, conductivities, and Diffusion Coefficients, Sandia National Labs., Livermore, CA (USA), 1983. Report No. SAND86-8246.
[82] W.L. Grosshandler, RADCAL: A Narrow-Band Model for Radiation Calculations in a Combustion Environment, NIST, Gaithersburg, MD, 1993. Report No. 1402.
[83] Turbulent Non-premixed flame workhop, https://tnfworkshop.org/radiation/ (accessed 11/18/2023).

[84] W.H. Dalzell, A.F. Sarofim, Optical Constants of Soot and Their Application to Heat-Flux Calculations, J.. Heat. Transf. 91 (1969) 100–104.
[85] T. Kathrotia, U. Riedel, A. Seipel, K. Moshammer, A. Brockhinke, Experimental and numerical study of chemiluminescent species in low-pressure flames, Appl. Phys. B 107 (2012) 571–584.
[86] J.M. Samaniego, F.N. Egolfopoulos, C.T. Bowman, CO2* Chemiluminescence in premixed flames, Combust. Sci..Technol. 109 (1995) 183–203.
[87] A. Hossain, Y. Nakamura, A numerical study on the ability to predict the heat release rate using CH* chemiluminescence in non-sooting counterflow diffusion flames, Combust. Flame 161 (2014) 162–172.
[88] A. D'Anna, M. Commodo, M. Sirignano, P. Minutolo, R. Pagliara, Particle formation in opposed-flow diffusion flames of ethylene: an experimental and numerical study, Proc. Combust. Inst. 32 (2009) 793–801.
[89] M.K. Ashour, F. Khosravi, F. Carbone, A Planar Mixing Layer Flame (PMLF) configuration to perform spatially resolved High-Resolution Differential Mobility Analysis (HR-DMA) in diffusion flames, in: Presented at the 41st Annual Conference of the American Association for Aerosol Research (AAAR), Portland, Oregon, 2023. October 2-6, 2023.
[90] E. Ranzi, A. Frassoldati, R. Grana, A. Cuoci, T. Faravelli, A.P. Kelley, C.K. Law, Hierarchical and comparative kinetic modeling of laminar flame speeds of hydrocarbon and oxygenated fuels, Prog. Energy Combust. Sci. 38 (2012) 468–501.
[91] F.N. Egolfopoulos, N. Hansen, Y. Ju, K. Kohse-Höinghaus, C.K. Law, F. Qi, Advances and challenges in laminar flame experiments and implications for combustion chemistry, Prog. Energy Combust. Sci. 43 (2014) 36–67.
[92] S.K. Friedlander, Smoke, Dust and Haze: Fundamentals of Aerosol Dynamics, Oxford University Press, New York, USA, 2000.
[93] Z. Li, H. Wang, Thermophoretic force and velocity of nanoparticles in the free molecule regime, Phys. Rev. e 70 (2004) 021205.
[94] J.A. Miller, C.F. Melius, Kinetic and thermodynamic issues in the formation of aromatic compounds in flames of aliphatic fuels, Combust. Flame 91 (1992) 21–39.
[95] P.R. Westmoreland, A.M. Dean, J.B. Howard, J.P. Longwell, Forming benzene in flames by chemically activated isomerization, J. Phys. Chem. 93 (1989) 8171–8180.